The Strike Point Pattern on the Local Island Divertor in LHD

Shigeaki Jimbo

DOCTOR OF PHILOSOPHY

Department of Fusion Science

School of Physical Sciences

The Graduate University for Advanced Studies

2004 (School Year)

Abstract

The Local Island Divertor (LID) is one of the divertor concepts involved in the Large Helical Device (LHD) configuration and it utilizes an $m/n = 1/1$ island formed at the edge region of the LHD. The LID has been proposed to control the edge plasma of the LHD. Control of the edge plasma by means of the LID aims to achieve high temperature divertor operation (HT-operation). It is important to investigate whether or not the particle flux, in particular the ion flux, cross the island separatrix is successfully guided to the rear side of the island where the target plates are placed to receive the particle load. If the particles strike on the front part of the LID head, then the particles neutralized on the front part cannot be pumped out, because the front part is not covered by the pumping duct. Thus, optimization of the particle orbits in the island region is the key to realize HT-operation by means of the LID. In here performance of LID is defined in the ratios of the test particles striking the front and rear parts of LID head. In order to estimate the performance of the LID system, we should investigate strike point patterns on the LID head.

Assuming HT-operation is achieved it is expected that the neoclassical effect on the edge transport becomes important. Since the edge plasma in HT-operation is collisionless, the orbits of charged particles become complex compared to the field lines; i.e. the effect of the Coulomb collision causes the transition between a passing particle orbit in the 3D field line structure and a trapped particle orbit in toroidal and helical ripples (localized and/or blocked particle orbits). Thus, according to the ratio of the mean free path to the connection length, the pitch angles of the particles which contribute the particle flux to the LID head is expected to vary; in the present study it is called the neoclassical effect on the edge transport phenomena. Here, the connection length is given as a length along

a field line connecting the core region to the LID head estimated as $Lc = 100$ m. Monte Carlo simulation based on test particle representation is carried out in order to investigate on strike point patterns of ions on the LID head in the 3D field line structure, the edge plasma transport under HT-operation.

The strike point patterns on the LID head have been numerically observed by tracing the orbits of the guiding centers in the fixed magnetic field under the effects of the Coulomb collisions and the anomalous diffusion.

The change in strike point pattern was seen according to the change in λ_{mfp}/L_c. When the mean free path λ_{mfp} is estimated as $\lambda_{mfp}/L_c = 3$, the strike point pattern becomes almost symmetric, and peak of strike point pattern corresponds to the intersection of the island separatrix on the LID head, where the collision frequency of the edge plasma is estimated as $\nu = 9.0 \times 10^3\ s^{-1}$. In this case, the passing particles mainly contribute the particle flux to the head, thus the particles contributing the transport follow the orbits along field lines of the island separatrix. When the mean free path λ_{mfp} is estimated as $\lambda_{mfp}/L_c = 0.03$, the particles escaping into the island region suffer the pitch angle scattering sufficiently and are carried to a far region from the island separatrix. In this case the particles strike mainly the inside in front of the LID head and decrease the number of particles that reach rear side separatrix. When the mean free path λ_{mfp} is estimated as $\lambda_{mfp}/L_c = 0.3$, the strike point pattern becomes not symmetric, and peak of the strike point pattern is located at the edge of the head. In this case, the particles transit between a passing particle orbit and a trapped particle orbit in toroidal and helical ripples. So trapped particle orbits escaping into the island region suffer the pitch angle scattering and are carried to inside of region from the island separatrix. Passing particle orbits move along field lines of the island. Around the head, $B \times \nabla B$ motion of particles are downward. Therefore, the particle that approaches the head from the upper part reaches the head easily, and the particle that approaches from the lower side doesn't reach the head easily. Broken symmetry of strike point pattern is caused by this effect.

The neoclassical effect plays the important role in determining the strike point patterns on the LID head. The performance is improved according to the rise of λ_{mfp}/L_c. The above results are not easily treated in fluid representation.

Acknowledgement

First of all, I would like to thank my supervisor, Professor Masao Okamoto for having kindly advised me throughout my doctor course. Moreover, I wish to thank him for providing me the opportunity to study plasma physics in here.

I am also grateful to Dr. Ryutaro Kanno for his helps over all of my academic activity. The result that I had achieved was not achieved without his help.

As concerning this work, I would like to thank Dr. Hisanori Takamaru for giving useful suggestions, espacially on the numerical calculation method.

I would like to thank Dr. Shinsuke Satake for his many helps including valuable suggestions and discussions.

I wish to express my gratitude to Professor Nobuyoshi Ohyabu who helped me to understand vital point of the divertor. I am also grateful for useful coments and offer of data concerning LID from Dr. Tomohiro Morisaki and Dr. Suguru Masuzaki. I am thankful to Professor Hideo Sugama for reading the manuscript and making useful comments and suggestions. I would like to acknowledge all the staffs in Theory and Data Analysis Division and Theory and Computer Simulation Center in NIFS for their friendliness and for having given me a lot of suggestions on my work.

Contents

Chapter 1

Introduction

1.1 Characteristic of edge plasma

It is necessary to reduce the interaction of the plasma and the wall to maintain good confinement of the high temperature plasma, and the plasma should be away from the wall. In magnetic plasma confinement system, the separation achieved by using nested magnetic surfaces which are closed in themselves is considered to avoid direct loss of particles moving along magnetic field lines. However, the plasma confinement using nested magnetic surfaces is not perfect. The Coulomb collision and various instabilities cause the particle and energy transport across the magnetic field, and they lead to contact with the wall. A direct interaction of the plasma and the wall generates impurities. The infiltration of impurities to the core plasma causes a large radiation loss, and the radiation loss cools the core plasma temperature. In addition, the dilution of the density of the fuel is caused and the heating efficiency becomes worse.

1.1.1 General function of divertor

In order to control the contact of the plasma and the wall and to avoid mixing impurities with the plasma, the edge region of the magnetic field containing the nested flux surfaces needs to be appropriately modified. In the toroidal devices like tokamaks, this is most often achieved either by superimposing an additional magnetic field at the plasma

periphery that diverts the plasma onto target plates in separate chamber. The study of the divertor physics has developed mainly on the tokamaks for ITER, but are relevant for any other reactor class device.

In divertor configuration, the ion particle flux and heat flux from core plasma go across the separatrix, and they flow into the region surrounding the core plasma. In this region, plasma particle flux and heat flux are transported according to the field line, and lead to divertor plates. This balance between perpendicular diffusion across the separatrix and rapid parallel ion flow to the divertor plates in divertor configuration establishes a narrow boundary layer or scrape-off layer (SOL) surrounding the core plasma. The flow along field lines strongly reduce the radial plasma fluxes diffusing toward the vessel walls and the effects of their interactions with the wall materials. The reduced amounts of impurity atoms released from the wall are ionized in the SOL afterwards, and become part of the parallel flow in this region. The SOL region thus shields the core plasma from wall impurity influxes and shields the vessel wall from radial plasma fluxes. As for the divertor configuration, the experiment was conducted first in Japan, and the control of impurities has been confirmed[1].

However, the intense flow cause the concentration of the particle and heat loads to divertor plates. In future reactor grade devices such as ITER, the high heat flux may be beyond the power-handling ability of the divertor material, and heat removal becomes one of the critical issues. Moreover, the importance of plasma density control and helium ash, ion impurities exhaust has been revealed from a recent research for the steady state operation[2, 3]. Thereby, the divertor configuration must have the reliable function of control of particle, and removal of impurity and heat.

In addition to particle and impurity control, and power exhaust, another important function of a divertor configuration is to improve the plasma performance through controlling the edge plasma conditions. In ASDEX the improvement of not only the impurity control but also the confinement energy, namely H-mode, has been discovered by the divertor configuration[4]. The H-mode plasma profile and conditions at the plasma edge strongly influence the plasma operation and energy confinement[5]. Therefore, the control of the edge plasma play a important role to the improvement of the energy confinement.

Different edge plasma operations have been studied to achieve the optimization of edge conditions, and thereby, the optimization of the core plasma performance.

1.1.2 Divertor operations

In the conventional divertor operation, strong temperature and density gradients develop in the SOL plasma along the magnetic field lines. The operation creates a cold dense radiative plasma near the divertor plates and creates a relatively high temperature and low density plasma surrounding the core plasma. The low temperature plasma in contact with the divertor plates reduces plate sputtering and the high temperature of SOL plasma in contact with the core plasma is necessary for H-mode. Such an edge plasma condition allows simultaneous achievement of the radiative cooling and H-mode, as seen in DIII-D[6, 7] and ASDEX-U[8]. However, this simultaneous achievement of the radiative cooling and H-mode, is not enough and still critical issue for future reactor grade devices. In the conventional divertor operation, the plasma in the SOL region is highly collisional, i.e. the particle Coulomb mean free path λ is less than the parallel dimension L of the SOL.

On the other hand, one of the advanced divertor operation, high temperature divertor plasma operation, has been proposed which is expected to enhance the core energy confinement and eliminates the heat removal problem of a reactor grade device [9, 10]. In this operation, the temperature of the divertor plasma is maintained to be very high by avoiding particle recycling at the divertor plate. Such a high temperature divertor plasma is achieved by efficient pumping in the divertor. An elevated divertor temperature will lead to an improvement of the core plasma, as observed in H-mode discharges. The validity of this concept has been demonstrated somewhat by JT60-U discharges with low recycling, in which ion temperature of SOL plasma is raised up to several keV through pumping by the boron coated wall and a record high value of $n\tau_E T$ has been achieved. This type of operation is planned to be pursued further in the large helical device (LHD). For reactor grade devices, the divertor field lines, however are needed to be guided into remote chambers outside of the coil cage, where the magnetic field is weak and large divertor channel is available, thereby reliable heat removal field and efficient pumping can be achievable. For helical devices, such a divertor magnetic configuration can be formed easily by proper

arrangement of the coil[11]. In contrast to the conventional divertor operation, the SOL plasma is collisionless in the high temperature divertor operation, namely, $\lambda \gg L$.

1.2 Divertor study in LHD

The LHD is the large heliotron device with poloidal/troidal period numbers of 2/10, major and averaged plasma minor radius of 3.9 and 0.6 m, respectively[12]. The LHD offers a great opportunity to study currentless plasmas in the heliotron configuration. Full steady state operation is expected, using superconducting coils in addition to a full helical divertor. Steady state plasma operation, essential to magnetic fusion reactors, is an inherent advantage of heliortons over tokamaks. The LHD has started its experiments since 1998 and explored a new operational regime for helical device[13]. The major goal of the experiment is to achieve high quality helical plasmas relevant to a fusion reactor, requiring a divertor system with high performance. The divertor must remove heat flow from the core safely and simultaneously improve the core energy confinement. It is the same as other devices also in LHD.

Two completely different divertor magnetic geometries are to be employed for diverting the outward flowing plasma in LHD. The Helical Divertor (HD) is equivalent to the tokamak double null divertor. In this configuration, a closed surface region is surrounded by a stochastic region generated by overlapping of the naturally existing island[10, 14]. The field lines escaping from this region pass through thin, curved surface layers, peculiar to this type divertor geometry, before reaching the X-point and then the divertor plate.

The Local Island Divertor (LID) is the other divertor configuration, which utilizes a magnetic island with $m/n = 1/1$ for plasma division[15, 16, 17, 18]. The details are described in the following subsection.

In LHD divertor experimental program, one of the new boundary control scheme, namely simultaneous achievement of H-mode and radiative cooling (SHC operation), has been proposed[19], which could allow simultaneous achievement of the H-mode type confinement improvement and edge radiative cooling with wide heat flux distribution. In the proposed configuration, the $m/n = 1/1$ island sharply separates the plasma confining region from the open 'ergodic' boundary. The connection length(between the point just outside of the last closed magnetic surface and the divertor plate) is 200m. It may be equivalent to tokamak poloidal divertors with long divertor channels. When collision with

neutral particle is minimized by a baffle, high degree of openness (i.e. dominance of the parallel transport over the perpendicular transport) in the ergodic boundary makes the plasma pressure constant along the field line, which in turn separates low density plasma just outside the plasma configuration region (the key external condition for achieving a good H-mode discharge) from very high density, cold plasma near the wall (required for effective radiative cooling). In this approach, the magnetic configuration is the same as that of LID, the divertor head has not been inserted, and pumping is not essential. Of course, high density, radiative cold plasma operation and high temperature operation are also being considered

1.2.1 Local Island Divertor

Control of the edge plasma by means of the LID is aimed to realize high temperature divertor operation (HT-operation) [20, 21]. The advantage of LID over a HD is the technical ease of pumping in the closed system, since recycling is toroidally and poloidally localized in a small region. LID is one of the divertor concepts in LHD configuration, and it utilizes an $m/n = 1/1$ magnetic island formed at the edge region of the LHD, where m and n are poloidal and troidal mode numbers, respectively. No closed surface exists any further, outside the island. The principle of LID is as follows. Particles diffusing from the core region cross the island separatrix and flow along the periphery of the island. After several toroidal turns, they reach the rear side of the island where the divertor head is placed and strike its backside on which they are neutralized. Since the divertor head is inserted deeply in the island, the leading edge of the head is safe from the high heat flux strike, as shown in Fig. 1.1. Particles recycled there are pumped out efficiently by the strong pumping system with a pumping duct integral into the closed divertor configuration.

To operate LID as an ideal divertor, as mentioned in this section, particles diffusing form core region should be directed to the backside of the divertor head along the island periphery. However, in the actual plasmas, there is a finite cross field diffusion due to collisions or anomalous transport, by which trajectories of particle are deviated from magnetic surfaces of the island periphery. If the deviation from field lines is too large,

particles are not guided by the island and directly strike the leading edge. In order to estimate the performance of the LID system, we should investigate strike point patterns on the LID head, of which pumping efficiency is required to be $> 30\%$. It is important to investigate whether or not the particle flux, in particular the ion flux crossing the island separatrix, is successfully guided to the rear side of the island where the target plates are placed to receive the particle load [17, 18, 20]. If the particles strike on the front part of the LID head, then the particles neutralized on the front part cannot be pumped out, because the front part is not covered by the pumping duct, see Fig. 1.1. Thus, optimization of the particle orbits in the island region is one of the key issues to realize HT-operation by means of the LID.

1.3 Several remarks on relevant study

To study the physics of the improvement of the confinement by control of the edge plasma by means of LID has been proposed, in advance of the LHD application, experimental studies in compact helical system (CHS) which is a small heliotron device were performed to prove the LID function[22, 23, 24]. From the theoretical approach, numerical simulations were carried out to optimize the geometrical configurations of the magnetic field structure and hardware components, e.g. divertor head and pumping duct, for maximum pumping efficiency[25]. Furthermore, the effect of the LID magnetic configuration on plasma performance was studied without the divertor head[26]. The summary of resultants of these studies are as follows. In the LID experiment of CHS, the particle flow was observed to be guided to the back side of the externally created magnetic island along field lines, and pumped out with high pumping efficiency, and observed a modest improvement of energy confinement, which could be due to the edge plasma control by the local island divertor. In order to estimate the diffusion coefficient appropriate to the LID operation, a field line tracing code coupled to a random walk process, i.e. Monte Carlo technique, was employed to simulate the diffusive particle behavior in LHD. For the case where $D = 0.1\mathrm{m}^2/\mathrm{s}$, the leading edge is safe from direct strikes by diverted particles which are well directed to the backside of the head. In this case, LID works as an island divertor. For the case where $D = 1.0\mathrm{m}^2/\mathrm{s}$, the leading edge is exposed to high heat loads resulting in a danger situation. In this case, LID acts like a conventional limiter. From the results of the simulation, it is found that D is recommended for LID to be less than $< 0.1\mathrm{m}^2/\mathrm{s}$. Fortunately, D in LHD has been found to be $\approx 0.1\mathrm{m}^2/\mathrm{s}$ [27]. In the LID configuration experiment, the decrease in n_e and the prevention of impurity penetration into the core plasma were attributed experimentally to the existence of the ergodic layer in the LID configuration, where neutral particles are ionized and flow along the field lines to the wall. These are fundamental function of the LID configuration. By using the divertor head, the reduction of n_e will be enhanced remarkably. Thus, combined with core fueling, the LID has the feasibility of realizing a low recycling operational mode, in other words, high-temperature edge plasmas, which could lead to a significant energy

confinement improvement in LHD.

The analysis of the edge plasma that used a fluid technique started recently. A 3D self-consistent Monte Carlo code EMC3 has been developed, aimed at investigating the edge transport in stellarators in the presence of island[28]. The code solves a simplified version of the 3D time-independent plasma fluid equations. The code provides a high flexibility in the grid construction, so that it can be easily adapted to any complicated 3D edge topology of stellarators. Coupled to EIRINE code[29], the EMC3 code simulates self-consistently the plasma and neutral transport in a full 3D space. Alternatively, the code can be used as a fit procedure to estimate the transport parameters by matching the local experimental data. In a first application to the proposed divertor configuration in W7-AS, the code predicts a density rise consistent with high recycling conditions in the islands. Similar behaviour has been observed experimentally in W7-AS with the inboard target configuration. The code results are supported by different diagnostics.

In study of LID a good result has been obtained from a preliminary experiment, and the analysis by the simulation code has been started. However, the research that accurately considers the drift motion and the pitch angle scattering has not be done.

1.4 Analyses of the edge plasma transport

Analyses of the edge plasma transport are classified in two types: fluid and particle representations. When collisionality is strong, it is known that the fluid approximation based on Braginskii's fluid equations is valid [30]. In order to solve directly the fluid equations in the three-dimensional (3D) field line structure with the $m/n = 1/1$ island and ergodic zone, two kinds of differential operators along and across a field line, i.e. $\nabla_{\parallel}$ and $\nabla_{\perp}$, are needed. It is not so easy to appropriately realize the operators in the 3D field line structure. Accordingly, one may consider that the Feynman-Kac formula is stretched to numerically solve the fluid equations by using the corresponding stochastic differential equations [31, 28, 32]. However, in this method there is difficulty in numerically solving the fluid equations with the nonlinear terms[33]. Furthermore, in HT-operation it is expected that the neoclassical effect on the edge transport becomes important. Since the edge plasma in HT-operation is collisionless, the orbits of charged particles become complex compared to the field lines; i.e. the effect of the Coulomb collision causes the transition between a passing particle orbit in the 3D field line structure and a trapped particle orbit in toroidal and helical ripples (localized and/or blocked particle orbits). Thus, according to the ratio of the mean free path to the connection length, the pitch angles of the particles which mainly contribute the particle flux to the LID head are expected to vary [33, 34]; in the present study we call it the neoclassical effect on the edge transport phenomena. Here, the connection length is given as a length along a field line connecting the core region to the LID head. In the investigation of strike point patterns on the LID head in the 3D field line structure, the Monte Carlo simulation based on test particle representation has an advantage of appropriately treating the edge plasma transport under HT-operation [33].

1.5 Purpose and Outline of this study

The improvement of the confinement is one of the most important issues in the study of the fusion plasma. The control of the edge plasma by means of the LID aims to clarify physics of control of the edge plasma and the improvement of confinement. In the actual plasmas, there is a finite cross field diffusion due to collisions or anomalous transport, by which trajectories of particle are deviated from magnetic surfaces of the island periphery, as described in the previous section. Therefore, the research of the characteristic of LID that consider such efficacy is important. Monte Carlo simulation based on test particle representation is carried out in order to investigate the neoclassical effect on a strike point pattern of ions on the LID head in the LHD configuration. The pattern on the LID head is numerically observed by tracing the guiding center orbits of the test particles under effects of the Coulomb collision and anomalous diffusion. In Chapter 2, we describe the model. Chapter 3 shows simulation results. Finally, in Chapter 4, the main results of this study are summarized.

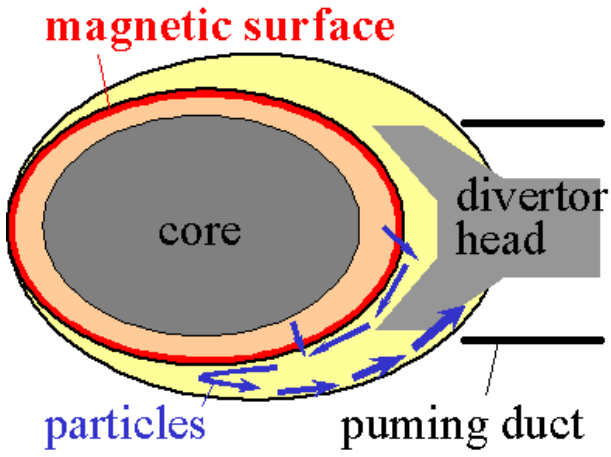

Figure 1.1: Schematic view of LID. Diverted particles do not hit the leading edge of the divertor head.

Chapter 2

Test particle simulation for edge transport

2.1 Model description

In this section, the model to investigate the neoclassical effect on a strike point pattern on LID head is described.

We consider that the plasma is confined in the LID configuration, and the LID head has been inserted in the island. Let us consider that the strike point pattern of LID head is decided by the ion flux from the core plasma. Temperature and density of the Maxwellian background plasma are uniform in the edge region including the island and they set the collisionality. According to collisionality, the particle orbits contributing the particle flux from the core region to the LID head vary. We assume that the pitch angle scattering is dominant compared with the other effects of the collisions. Here we neglect the effect of the electric field, but when considering the radial diffusion by anomalous transport, we assume that it is caused by electrostatic turbulence. The effect of neutrals on determining the strike point patterns is relatively negligible compared with the other effects because of efficient pumping. The particles that reach the head and the wall are completely absorbed there. The pattern on the LID head is numerically observed by tracing the guiding center orbits of the test particles under effects of the Coulomb collision and anomalous diffusion. In the calculations of the orbits, we consider a vacuum magnetic field of the LHD, where

the magnetic axis is located at $R_{\rm ax} = 3.6$ m and the strength of magnetic field at the axis is $B_{\rm ax} = 3$ T. The connection length is length of field line from the core region to the LID head and it is estimated as $L_{\rm c} \approx 100$ m.

2.1.1 Equations of motion

The variational principles of guiding center motion are given by Littlejohn[35]. The variational method have the advantages of being invariant under arbitrary coordinate transformations, and that the invariance associated with symmetries follows transparently from the independence of the Lagrangian of the corresponding symmetry coordinates.

The general form of the variational principle is written by

$$\delta \int L dt = 0, \tag{2.1}$$

where the L is the gyroaverage of the Lagrangian of the particle

$$L = (\mathbf{z}, \dot{\mathbf{z}}, t) = \gamma \cdot \dot{\mathbf{z}} - H, \tag{2.2}$$

written in an arbitrary coordinate system on phase space $\mathbf{z} = \mathbf{z}(\mathbf{q}, \mathbf{p}, t) = (z_i, i = 1, ..., 6)$, $\gamma = (\gamma_i, i = 1, ..., 6)$,and H are functions of $\mathbf{z}$ and t, given by

$$\gamma_i(\mathbf{z}, t) = \mathbf{p} \cdot \frac{\partial \mathbf{q}}{\partial \mathbf{z}} \tag{2.3}$$

$$H(\mathbf{z}, t) = H_{can} - \mathbf{p} \cdot \frac{\partial \mathbf{q}}{\partial t} \tag{2.4}$$

where H_{can} is the usual Hamiltonian in terms of canonical variables $(\mathbf{q}, \mathbf{p}) = (q_i, p_i, i = 1, 2, 3)$. The equations of motion will always follow by varying the integral of $L(\mathbf{z}, \cdot\mathbf{z}, t)dt$. The variations of all six phase space coordinates $\mathbf{z}$ are to be considered independent during the variational process, even if a functional dependence should result through the equations of motion. In the case of a particle in an electromagnetic field, the canonical Hamiltonian is

$$H_{can}(\mathbf{q}, \mathbf{p}, t) = \frac{1}{2m} \left(\mathbf{p} - \frac{e}{\epsilon} \mathbf{A}(\mathbf{q}, \epsilon t) \right)^2 + e\Phi(\mathbf{q}, \epsilon t), \tag{2.5}$$

where ϵ is the adiabatic ordering parameter which physically represents the ratio of gregarious to scale length, and adiabatic ordering assume the slow change of the corresponding parameter. Let $\mathbf{z} = (\mathbf{x}, \mathbf{v})$,where $\mathbf{x}$ is the particle position, and $\mathbf{v}$ is the particle velocity. Then,

$$L = \left(\frac{e}{m\epsilon}\mathbf{A}(\mathbf{x}, \epsilon t) + m\mathbf{v}\right) \cdot \dot{\mathbf{x}} - \left(e\Phi(\mathbf{x}, \epsilon t) + \frac{mv^2}{2}\right) \tag{2.6}$$

Note that $\mathbf{v}$ is considered independent of $\dot{\mathbf{x}}$, even though $\mathbf{v} = \dot{\mathbf{x}}$ follows from the equation of motion. This is because the variational principle selects the physical motion out of all conceivable motions, as the one to make the action integral stationary. Let us write $u = v_{\|}$ and $w = v_{\perp}$, and decompose the particle velocity $\mathbf{v}$ according to

$$\mathbf{v} = u\hat{b} + w\hat{c} \tag{2.7}$$

where $\hat{c}$ is a perpendicular unit vector. At lowest order,$u, \hat{b}$,and w are purely averaged, but $\hat{c}$ is purely oscillatory. Similarly decompose position $\mathbf{x}$ according to

$$\mathbf{x} = \mathbf{X} + \frac{\epsilon m w \hat{a}}{eB} \tag{2.8}$$

where $\mathbf{X}$ is the guiding center position,

$$\hat{a} = cos\theta\hat{e}_1 - sin\theta\hat{e}_2 \tag{2.9}$$

$$\hat{c} = -sin\theta\hat{e}_1 - cos\theta\hat{e}_2 \tag{2.10}$$

where, θ is the instantaneous gyrophase, where $\hat{a} = \hat{b} \times \hat{c}$,and $\hat{e}_{1,2}(\mathbf{x}, \epsilon t)$ are some arbitrary pair of perpendicular unit vectors, satisfying $\hat{e}_1 \times \hat{e}_2 = \hat{b}$. Then the equation of motion are invariant under the substitution $L \to L + dS/dt$, i.e. under

$$\gamma_i \to \gamma_i + \frac{\partial S}{\partial \mathbf{z}}, \quad H \to H - \frac{\partial S}{\partial t},$$

with $S = S(\mathbf{x}, t)$ an arbitrary scalar, gives possibility to write the oscillatory part of the partial Lagrangian approximately as a total time derivate

$$L - \langle L \rangle = \frac{eB}{m}\frac{\partial S}{\partial \theta} \approx \frac{dS}{dt} + O(\epsilon), \tag{2.11}$$

so that this oscillating part can be eliminated term by term from the Lagrangian. The results is

$$L'(\mathbf{X}, \dot{\mathbf{X}}, v_\parallel, \mu, \theta) = \langle L \rangle = e\mathbf{A}^* \cdot \dot{\mathbf{X}} + \frac{m}{e}\mu\dot{\theta} - H', \tag{2.12}$$

where

$$H' = e\Phi + \mu B + \frac{m}{2}v_\parallel^2, \quad \mu = \frac{mv_\perp^2}{2B}$$

and $\mathbf{A}^*$ is the effective magnetic potential

$$\mathbf{A}^* = \mathbf{A} + \rho_\parallel \mathbf{B}, \quad \rho_\parallel = \frac{mv_\parallel}{eB} \tag{2.13}$$

defined by the pseudo-magnetic field $\mathbf{B}^* = \nabla \times \mathbf{A}^*$. The quantity $\rho_\parallel$ is the parallel gyro-radius. The Euler-Lagrange equations for the six independent variables $\mathbf{z} = (\mathbf{X}, v_\parallel, \theta, \mu)$ are given by

$$\frac{d}{dt}\left(\frac{\partial L}{\partial \dot{\mathbf{z}}}\right) - \left(\frac{\partial L}{\partial \mathbf{z}}\right) = 0 \tag{2.14}$$

i.e. explicitly the set of the drift equations is

$$\begin{aligned}
\dot{\mathbf{X}} &= \frac{v_\parallel}{B_\parallel^*}(\mathbf{B} + \frac{m}{e}v_\parallel \nabla \times \mathbf{b}) \\
\dot{\mathbf{X}}\mathbf{b} &= v_\parallel \\
\dot{\mu} &= 0 \\
\dot{\theta} &= \frac{eB}{m}
\end{aligned} \tag{2.15}$$

where $\mathbf{b} = \mathbf{B}/B$, and $B_\parallel^* = B + \mathbf{b} \cdot \nabla \times (\mathbf{b}mv_\parallel/e)$

Finally, if the effects of anomalous diffusion and collisions with charged particles, neutrals, solid surfaces, etc. are neglected, the guiding center motion is expressed as [33, 35]

$$\dot{\mathbf{X}} = \mathbf{v} = \frac{1}{B_\parallel^*}\left[v_\parallel\left(\mathbf{B} + \frac{m}{eB}v_\parallel \nabla \times \mathbf{B}\right) + \left(\frac{\mu}{e} + \frac{m}{eB}v_\parallel^2\right)\mathbf{b} \times \nabla B\right], \tag{2.16}$$

$$\dot{v}_\parallel = -\frac{\mu}{mB_\parallel^*}\left(\mathbf{B} + \frac{m}{eB}v_\parallel \nabla \times \mathbf{B}\right) \cdot \nabla B, \tag{2.17}$$

$$\dot{\mu} = 0, \tag{2.18}$$

Here we neglect the effect of electric field.

2.1.2 Pitch angle scattering

The test particle transport is evaluated by the solution of the gyro-phase averaged Boltzmann equation [36].

$$\frac{\partial f}{\partial t} + \mathbf{v} \cdot \nabla f = C(f), \tag{2.19}$$

where $f = f(t, \mathbf{r}, E, \mu)$ is the particle distribution function, and $C(f)$ is the linearized pitch angle scattering due to Coulomb collisions. The energy E of each guiding center particle is conserved, and only the magnetic moment μ is changed by the Coulomb collisions. Instead of solving (2.19) directly, the Monte Carlo technique is used [37]. Equations for each guiding center particle equivalent to equation (2.19) consist of two parts: orbit part, and collision part.

The pitch angle scattering in equation (2.19) is expressed as

$$\frac{\partial f}{\partial t} = C(f) = \frac{\nu}{2} \frac{\partial}{\partial \lambda} \left((1 - \lambda^2) \frac{\partial f}{\partial \lambda} \right) \tag{2.20}$$

where the pitch angle $\lambda = v_{\|}/v$ is used instead of μ, and ν is the deflection frequency [37]. Knowing the solution of equation (2.20) with the initial condition $f(\lambda, t = 0) = \delta(\lambda - \lambda_0)$ a Langevin equation giving the same mean value of λ and standard deviation σ is constructed

$$\frac{d\lambda}{dt} + \nu\lambda = W(t) \tag{2.21}$$

where the collisional effect from the plasma background is splited up into two parts: a systematic part $\nu\lambda$, representing dynamical friction experienced by the particle and fluctuation part, W(t) which is modeled as a white noise source

$$\langle W(t) \rangle = 0, \;\; \langle W(t) W(t') \rangle = D\delta(t - t) \tag{2.22}$$

According to (2.20) the constant D is chosen to be $D = (1 - \lambda_0^2)\nu$. The general solution of the Langevin equation (2.21) is

$$\lambda(t) = \lambda_0 e^{-\nu t} + e^{-\nu t} \int_0^t W(t') e^{\nu t'} dt' \tag{2.23}$$

Corresponding the average value $\langle\lambda(t)\rangle$ (the first cumulant), and the square displacement (the second cumulant) are given by

$$\langle\lambda(t)\rangle = \lambda_0 e^{-\nu t}, \tag{2.24}$$

$$\sigma^2 = \langle\lambda^2(t)\rangle - \langle\lambda(t)\rangle^2 = \frac{1-\lambda_0^2}{2}\left(1-e^{-2\nu t}\right), \tag{2.25}$$

In the limit $\nu t \ll 1$ equation (2.25) and (2.25) become

$$\langle\lambda(t)\rangle \approx \lambda_0(1-\nu t) \tag{2.26}$$

$$\sigma^2(t) \approx (1-\lambda_0^2)\nu t \tag{2.27}$$

For a discrete time step Δt satisfying $\Delta t\nu \ll 1, \lambda$ is then change as

$$\lambda(t_n) = \lambda(t_{n-1})(1-\nu\Delta t) \pm \sqrt{(1-\lambda^2(t_{n-1}))\nu\Delta t}, \tag{2.28}$$

for one step from $t_{n-1} = (n-1)\Delta t$ to $t_n = n\Delta t$ [37]. The symbol $\pm$ indicates that the sign is to be chosen randomly, but with equal probability for plus and minus.

2.1.3 Anomalous diffusion

When an anomalous diffusion process in configuration space is considered as generating a perpendicular particle flux $\Gamma_{a\perp}$, which models electrostatic turbulence $(1/B_\parallel^*)\mathbf{b}\times\nabla_\perp\tilde{\Phi}$. Flux is expressed as

$$\Gamma_{a\perp} = -\overleftrightarrow{D}_a \cdot \nabla n_i$$

where $\overleftrightarrow{D}_a = D_a(\overleftrightarrow{I} - \mathbf{bb})$ denotes the tensor of the anomalous diffusion coefficient. The Fokker-Plank equation is obtained from the equation of continuity.

$$\begin{aligned}\frac{\partial n}{\partial t} &= \frac{\partial}{\partial x^i}\left(D_a^{ij}\frac{\partial n}{\partial x^j}\right) \\ &= -\frac{\partial}{\partial x^i}\left(n\frac{\partial D_a^{ij}}{\partial x^j}\right) + \frac{\partial^2}{\partial x^i \partial x^j}\left(nD_a^{ij}\right)\end{aligned} \tag{2.29}$$

The Langevan equation is given as follows.

$$dx^i = \frac{\partial D_a^{ij}}{\partial x^j}dt + \sigma^{ij}dW_j(t) \tag{2.30}$$

where

$$\sigma^{ij} = \sqrt{D_a}\left(\delta^{ij} - b^i b^j\right),$$

and $\overleftrightarrow{\sigma}_{\rm a} = \sqrt{(D_{\rm a})}(\overleftrightarrow{\rm I} - \mathbf{bb})$ satisfies the condition ${\rm D}_{\rm a}^{\alpha\beta} = \sigma_{\rm a}^{\alpha k}\sigma_{\rm a}^{\beta l} g_{kl}$, $\overleftrightarrow{\rm I}$ is the identity tensor, and g_{kl} is the metric coefficient. Electrostatic turbulence is express as

$$(1/B_{\parallel}^{*})\mathbf{b} \times \nabla_{\perp}\tilde{\Phi} \Rightarrow \nabla \cdot \overleftrightarrow{\rm D}_{\rm a} dt + \overleftrightarrow{\sigma}_{\rm a} \cdot d\mathbf{W}_t.$$

The motion in configuration space (2.16) can be modified to the following stochastic differential equation [33]:

$$d\mathbf{X} = \left\{\mathbf{v}(\mathbf{X}) + \nabla \cdot \overleftrightarrow{\rm D}_{\rm a}\left(\mathbf{X}\right)\right\} dt + \overleftrightarrow{\sigma}_{\rm a} \cdot d\mathbf{W}_t. \tag{2.31}$$

Here, we assume that the fluctuating electrostatic potential $\tilde{\Phi}$ itself is negligibly small $|e_i\tilde{\Phi}/K| \ll 1$, and that the effect of electrostatic turbulence on the parallel velocity is neglected, where K is the kinetic energy. The differential equations are solved by using the Monte Carlo techniques [38].

2.2 Simulation model

The simulation model is constructed from the model previously described. The orbits of the guiding centers of the test particles starting from a magnetic flux surface in the core region are traced in the fixed magnetic field under the effects of the Coulomb collision and anomalous diffusion. By tracing the orbits, the strike point pattern which is caused by ions supplied from the core region can be numerically observed. Realistic geometry of magnetic field and realistic shape of divertor head are necessary for an estimate of strike point of head. In subsection 2.2.1 we describe the magnetic field. The expression of divertor head is described in subsection 2.2.2. In subsection 2.2.3 we describe the initial condition and assumuptions.

2.2.1 Fixed magnetic field

The vacuum magnetic field data calculated by the MAGN code is used as a fixed magnetic field. We have used special type of non-orthogonal Eulerian coordinates used in the HINT code[39], namely helical coordinates. These coordinates consists of rectangular grids (u^1, u^2) on the u^3 =const. poloidal plane which rotates along the toroidal direction with the same pitch as that of external helical winding. The relation between the helical coordinates(u^1, u^2, u^3) and the Cartesian coordinates (X, Y, Z) is given as follows:

$$\begin{aligned} X &= (R_0 + u^1_* \cos hu^3 + u^2 \sin hu^3) \cos u^3, \\ Y &= -(R_0 + u^1_* \cos hu^3 + u^2 \sin hu^3) \sin u^3, \\ Z &= -u^1_* \sin hu^3 + u^2 \cos hu^3, \end{aligned}$$

with

$$u^1_* = u^1 + \delta$$

where h denotes the rotation number along ϕ direction, R_0 is the major radius, and δ is the amplitude of the deviation of helical geometrical axis from the generatrix circle.

2.2.2 Expression of Divertor head with computational grid

The Divertor head in this simulations is expressed by the block of computational grid. Fig. 2.1 shows the example of expressing the object in the block of computational grid. Fine grids are prepared around the head for this purpose, and the width between grids is 1cm in the direction of u^1 and u^2, and 0.5 degree in the direction of toroidal. The grid that composes the divertor head is selected by using the data of a genuine divertor head, and similar to real one as well as magnetic field data. The particle enclosed by this grid is counted as a particle that struck on the head, and the number of particles is distributed to the adjoining grid according to the distance. The three dimensional view of the LID head is shown in Fig. 2.2.

2.2.3 Initial condition

The assumptions we set here are 1) the test particles are protons, 2) all of the test particles are initially distributed on a magnetic flux surface located at the edge of the core region, which is very close to the island separatrix (see Fig. 2.3), 3) the temperature at the surface where the test particles originate is $T_i = 300$ eV, 4) the particles are mono-energetic $E = K = 300$ eV and the distribution of the initial pitch angles of the particles is uniform, 5) temperature and density of the Maxwellian background plasma are both uniform in the edge region including the island and they are decided to the value corresponding to given collisionality.

2.3 Benchmark test of MPPP code

In this study, we developed a Monte Carlo simulation code, the MPPP code (Monte carlo simulation for Particle-tracing in Peripheral Plasma), which is based on test particle representation. To benchmark the code against an analytic model, we calculate diffusion coefficient in tokamak configuration. The calculations are started (t=0) by introducing the monoenergetic (E=3keV) test electron ensemble of N=50000 independent electrons with randomly distributed poloidal troidal, and pitch angle ($\lambda[-1,1]$,where $\lambda = v_{\parallel}/v$) at flux surface with $r/a = 0.63(\iota/2\pi = 2/3)$. Each of the ensemble electrons evolutes independently according to equations which are solved by the 4th order Runge-Kutta procedure. To satisfy the energy constraint condition $E = const.$,the numerical step is chosen to be $dt \cong 5 \times 10^{-9}$s.

After each particle orbit step the Monte Carlo equivalent pitch angle operator is applied. The particularity of such a Monte Carlo procedure requires the checking of validity. In the neoclassical domain the system has two type of characteristic frequencies associated with the particle dynamics: the transit frequency of passing particle ν_t and bounce frequency of trapped particles ν_b. The characteristic times are $\tau_t(=\nu_t^{-1})$ for passing and $\tau_b(=\nu_b^{-1})$ for trapped particles, respectively. According to the relative magnitude among above characteristic frequencies (times) associated with particle dynamics and the deflection collision frequency ν (collision time,$\tau_c = \nu^{-1}$) due to the Coulomb collision associated with stochasticity, there are three type of collisionarity regime:

$$\begin{aligned}
&\nu \ll \nu_{be} \ll \nu_t \quad or \quad \tau_c \gg \tau_{be} \gg \tau_t : \quad \text{banana regime} \\
&\nu_{be} \ll \nu \ll \nu_t \quad or \quad \tau_{be} \gg \tau_c \gg \tau_t : \quad \text{plateau regime} \\
&\nu_{be} \ll \nu_t \ll \nu \quad or \quad \tau_{be} \gg \tau_t \gg \tau_c : \quad \text{Pfirsh-Schluter regime,}
\end{aligned} \tag{2.32}$$

where $\nu_{be} \equiv \varepsilon\nu_b = \tau_{be}^{-1}$ is the effective bounce frequency. Thus in the presence of collisions the characteristic frequencies and times at the initial flux surface are

$$\begin{aligned}
\nu_t &= \frac{\iota v}{2\pi^2 R} &&= 2.21 \times 10^6 s^{-1} : \quad \tau_t = \nu_t^{-1} = 4.35 \times 10^{-7} s \\
\nu_b &= \left(\frac{r}{R}\right)^{3/2} \nu_t &&= 2,30 \times 10^5 s^{-1} : \quad \tau_b = \nu_b^{-1} = 4.52 \times 10^{-6} s
\end{aligned} \tag{2.33}$$

where $v = \sqrt{2E/m}$

Diffusion coefficients is shown in Fig. 2.4. In the standard neoclassical theory, the radial diffusion is treated as the normal diffusive process. For each collisionality regime, the analytical diffusion coefficient is given by[40]

$$\begin{aligned} D_{PS} &= D_p \frac{\nu}{\nu_t} && : \text{for} \quad \nu_t \ll \nu \\ D_p &= 0.64 \times \frac{\rho^2 v}{2\pi R} = 1.24 \times 10^{-2} \mathrm{m}^2/\mathrm{s} && : \text{for} \quad \nu_{be} \ll \nu \ll \nu_t \\ D_b &= D_p \frac{\nu}{\nu_{be}} && : \text{for} \quad \nu \ll \nu_{be} \end{aligned} \tag{2.34}$$

where $\rho = mv/(eB)$ is the Larmor radius.

In Fig. 2.4 the analytical diffusion coefficient is plotted as the function of parameter ν (solid line).

An analytical solution and the calculation value were good agreement.

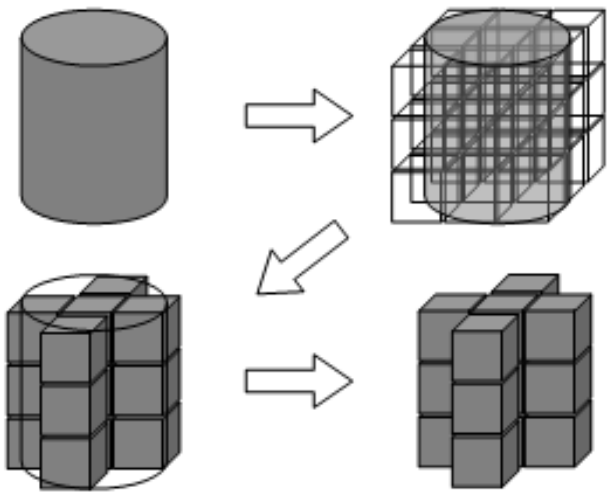

Figure 2.1: The example of the cylinder of the approximation in the block.

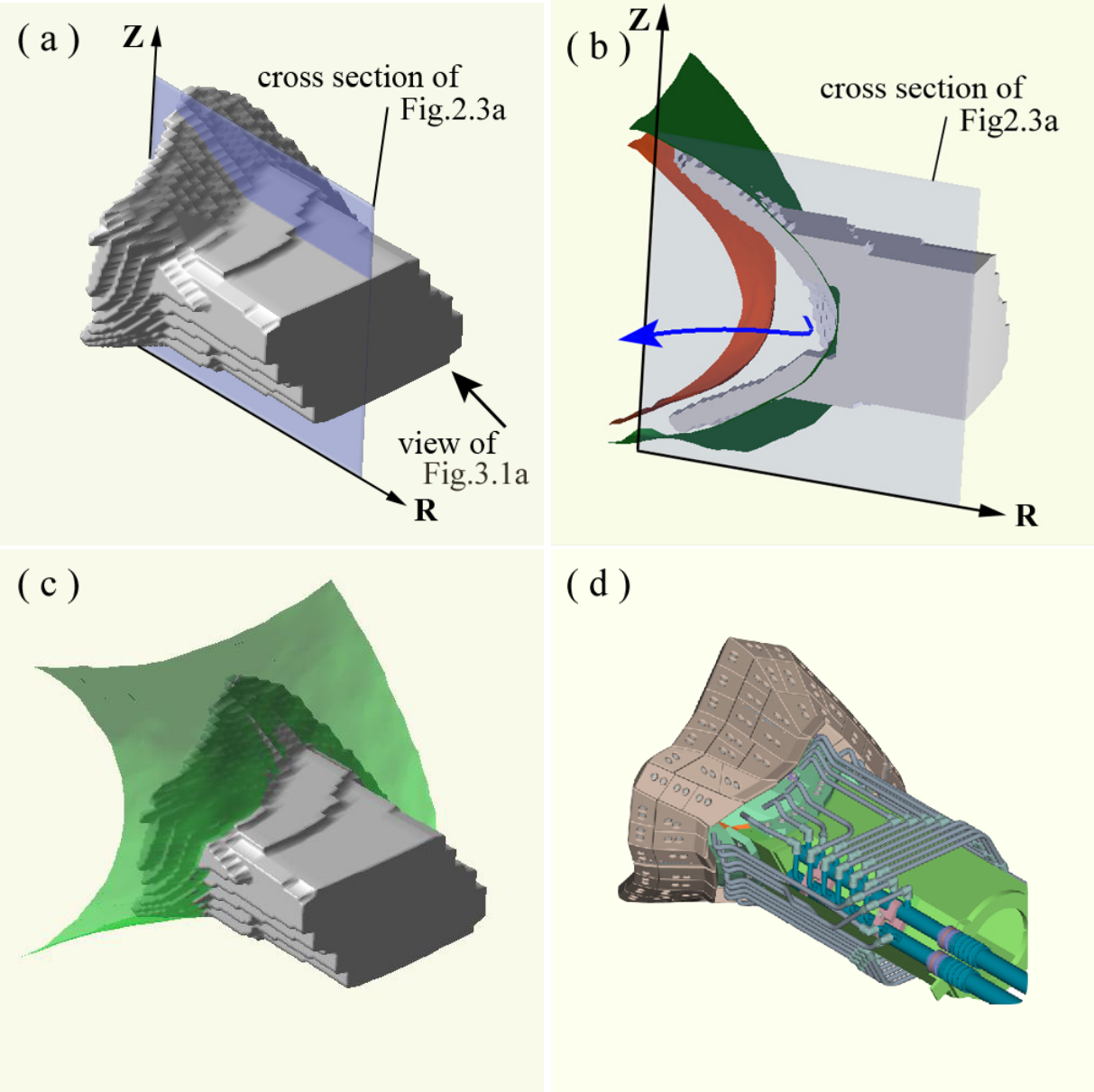

Figure 2.2: (a) The three dimensional view of the LID head. This view is the same as, for example, one seen in Fig. 3.1a. (b) The sectioned illustration of the LID head and the island separatrix, where orange and green surfaces indicate the front and rear sides of the island separatrix, respectively. A blue line indicates the orbit of the O-point of the $m/n = 1/1$ island. (c) Illustration of the LID head and the rear side of the island separatrix. This view is the same as one seen in the figure (a). (d) The figure (a) is the model of the LID head for the numerical simulations. The pumping duct is not depicted.

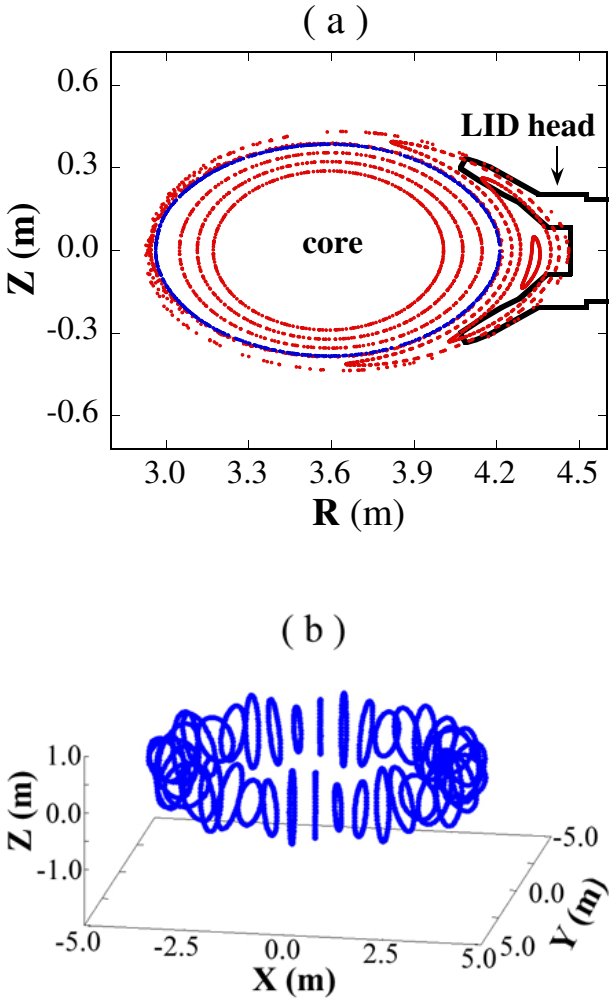

Figure 2.3: (a) Poincaré plots of field lines of the vacuum magnetic field with $R_{\mathrm{ax}} = 3.6$ m and sketch of the LID head on the horizontally elongated poloidal cross section. The magnetic flux surface where the test particles originate uniformly is shown by blue dots, see also (b).

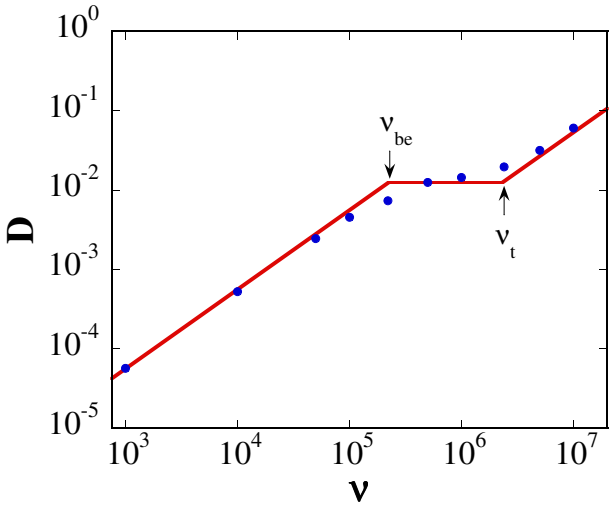

Figure 2.4: The comparison of the numerically and analytically calculated neoclassical diffusion coefficients for starting particles position $r/a = 0.63$ is shown. The values ν_{be} and ν_t correspond to the effective bounce frequency and transit frequency,respectively. The axes are plotted in log-log proportion.

Chapter 3

Neoclassical effect on strike point patterns

3.1 Feature of patterns

In this subsection, we describe how the orbits contributing the particle transport to the LID head vary according to the collisionality. The feature of the pattern by the $\lambda_{\rm mfp}/L_{\rm c}$ change is described. When the mean free path $\lambda_{\rm mfp}$ is estimated as $\lambda_{\rm mfp}/L_{\rm c} \approx 0.3$, we find that the peak of the strike point pattern is located at the edge of the head, as shown in Fig. 3.1, where the collision frequency of the edge plasma is estimated as $\nu = 8.4 \times 10^3$ $\rm s^{-1}$. We should note that the strike point pattern is not symmetric, see Figs. 3.1a and 3.1b. The distribution of $v_\parallel/v$ of the particles which strike the head is shown in Fig. 3.2a. The distribution of $v_\parallel/v$ for this case is not symmetric, as is also shown in Table 3.1. In order to understand asymmetrical distributions of the particles and positions of the peak point, we remove the LID head and calculate the incidence of the test particles moving across the cross section shown in Fig. 3.3a, then the distributions of the particles given in Figs. 3.3b and 3.3c are obtained just after the test particles starting from their initial positions go across the island separatrix. We find that the particle distribution in the rear side of the island has the peak inside the island separatrix (see Fig. 3.3b), and that the test particles escaping across the front side of the island separatrix carry a negative momentum having $v_\parallel < 0$ (see Fig. 3.3c). The yellow and red regions of the pattern

which corresponds to major region of the strike point pattern in Fig. 3.1 is explained by the particle distribution in Fig. 3.3b, because the part of the LID head indicated by the yellow and red regions is located inside the island separatrix as shown in Figs. 2.1b and 2.1c. The distribution of $v_{\parallel}/v$ in Fig. 3.2a is caused by the result in Fig. 3.3c. In the calculations carried out in the present paper, there is no source of the test particles, thus the asymmetrical distribution of the pitch angles shown in Fig. 3.4c becomes to be symmetric by the pitch angle scattering after sufficient time. If the source supplies the particles, however, the distribution of the pitch angles is maintained to be asymmetric. As a result, the existence of ion flow going upstream the magnetic field is expected at the boundary of the island. On the other hand, when the mean free path becomes larger, i.e. $\lambda_{\rm mfp}/L_{\rm c} \approx 3$ ($\nu = 9.0 \times 10^2$ s^{-1}), the strike point pattern is drastically changed as shown in Fig. 3.4. The pattern becomes almost symmetric, and the yellow region of the pattern corresponds to the intersection of the island separatrix on the LID head, see Figs. 2.1c and 3.4a. In this case, the passing particles mainly contribute the particle flux to the head as shown in Figs. 3.2 and 3.3, thus the particles contributing the transport follow the orbits along field lines of the island separatrix (see Fig. 3.3b). The symmetry of the pitch angle distribution is recovering, see Figs. 3.2a, 3.3c and Table 3.1. When the mean free path becomes very small, i.e. $\lambda_{\rm mfp}/L_{\rm c} \approx 0.03$ ($\nu = 7.8 \times 10^4$ s^{-1}), the test particles suffer the pitch angle scattering sufficiently and lose their initial memories when the particles go across the front side of the island separatrix. Thus, the distribution of $v_{\parallel}/v$ becomes almost symmetric and has gentle slopes, see Figs. 3.2a and 3.3c. The test particles intensively strike the edge of the LID head, see Figs. 3.5 and 3.3b. The particles that reached the head are classified from the viewpoint of the particle orbit and shown in Fig. 3.2b. The orbit is classified by the magnetic moment, it becomes as shown in the Table 3.3. The number of trapped particles increases with a decrease of $\lambda_{\rm mfp}/L_{\rm c}$. However, passing particle is dominant of all cases. To investigate it more in detail the example of the particle orbit is shown in next subsection.

3.1.1 Example of orbit

The examples of the particle orbits are shown. The case $\lambda_{\rm mfp}/L_{\rm c} \approx 3$ is shown in Fig. 3.6. The particles maintains the pitch angle for a long time for the low collision frequency, and turn toroidal many times and have not suffered trap. The passing particles flow along the periphery of the island and they reach the rear side of the island where the divertor head is placed and strike its backside. On the other hand, the trapped particles keep trapped and don't reach the head. Therefore, of course the passing particles mainly contribute the particle flux to the head, thus the particles contributing the transport follow the orbits along field lines of the island separatrix. In this case peak of strike point pattern corresponds to the intersection of the island separatrix on the LID head. There is both the particle orbit that strikes the head with negative pitch angle (see Fig. 3.6a) and the particle orbit that strikes the head with positive pitch angle (see Fig. 3.6b). The case $\lambda_{\rm mfp}/L_{\rm c} \approx 0.03$ is shown in Fig. 3.7. The particles frequently changes the pitch angle for high collision frequency, and trapped don't turn toroidal. Therefore, the particles escaping into the island region repeat bounce motion sufficiently and are carried to a far region from the island separatrix. In this case the particles strike mainly the inside in front of the LID head and decrease the number of particles that reach rear side separatrix, and peak of the strike point pattern is located at the edge of the head and there is both the particle orbit that strikes the head with negative pitch angle (see Fig. 3.7a) and the particle orbit that strikes the head with positive pitch angle (see Fig. 3.7b). The case $\lambda_{\rm mfp}/L_{\rm c} \approx 0.3$ is shown in Fig. 3.8. In this case the passing particles and the trapped particles exist together changing between the two. Therefore, when the particles trapped, they escape into the island region and suffer the pitch angle scattering and are carried to inside of region from the island separatrix, and when they become passing particles, they turn toroidal, and they reaches rear side of separatrix (see Fig. 3.8a). So peak of the strike point pattern is located at the edge of the head. In this case the particle orbits that strike the head with negative pitch angle are predominant.

The example of the particle orbit shows the followings. 1) The passing particles flow along the periphery of the island. And after several toroidal turns, they reach the rear side of the island where the divertor head is placed and strike its backside. 2) The trapped

particles repeat bounce motion, and they go into inside of island separatrix. They don't reach the rear side of the island, because they don't turn Taurus. Therefore, the strike point patterns on the LID head are varied according to collisionality. However, the reason why the pattern is not symmetric has not been understood yet. Considers asymmetric cause in the following subsections.

3.1.2 Effect of error field

One may suspect that the broken symmetry is caused by error magnetic fields, because the structure of the $m/n = 1/1$ magnetic island is perturbed by the error fields, see Fig. 3.9a. The island separatrix and the head are tighter than the lower side in the upper side of the head. Therefore, particles might reach the upper side of the head more easily than the lower side of the head. As far as we have examined, however, there is no significant difference in the results even if the error fields are canceled out, see Fig. 3.9b and Table 3.1. This is the same condition as Fig. 3.1 except that the error fields are canceled out, and the strike point pattern in this case is shown in Fig. 3.10. The broken symmetry is not caused by error magnetic fields. Other reasons exist.

3.1.3 Drift motion near head

In general, trapped particle orbits located at the upper side of the island drift into the head as shown in Figs. 3.11b. Here, the particle orbits shown in Fig. 3.11 are obtained by calculating the guiding center orbits without Coulomb collisions, where the initial value of $v_\parallel/v$ at the start points is $v_\parallel/v = -0.25$ in Fig. 3.11 and the LID head is removed in order to show the orbits of trapped particles in the island region. Even if the sign of $v_\parallel/v$ at the start points is set to be opposite, i.e. $v_\parallel/v = +0.25$ at the start points, the orbit behaves the almost same as the case of $v_\parallel/v = -0.25$. On the other hand, trapped particle orbits located at the lower side of the island go away from the head as shown in Figs. 3.11d. The example of the orbits that are located on symmetry position of the head are shown in Fig. 3.12. Actually, the upper particle has struck on the head after it bounces several times (see Fig. 3.12b) and the lower particle has gone away from the head

(see Fig. 3.12c). Of course, because passing particles are predominant, it is clear that the behavior of the particles of the reality are not the same. However, the number of particle that has struck on the head after it bounces several times increase according to an increase of collisionality. Thus, the asymmetrical pattern is expected. When the mean free path is very large ($\lambda_{\mathrm{mfp}}/L_{\mathrm{c}} \approx 3$), there is a very little probability of the transition between trapped and untrapped particle orbits. Thus, the passing particles mainly contribute the particle transport, as shown in Fig. 3.4c. The passing particles move along the island separatrix (see Fig. 3.4b), and the improvement of the performance is expected.

3.2 Estimation of performance of LID

From the ratios of the test particles striking the front and rear parts of the LID head in Table 3.1, we can estimate the performance of the LID system. If the particles strike on the rear part of the LID head, then the particles neutralized on the rear part can be pumped out, because the rear part is covered by the pumping duct. Therefore, the performance is defined here in the ratio of particles that strike the rear part to all particles that strike on the LID head. The performance is expected to be improved with increasing $\lambda_{\mathrm{mfp}}/L_{\mathrm{c}}$; i.e. the ion flux is guided mainly to the rear part of the head. Here, the front part of the head is shown in the front-view of Fig. 3.1d and the rear part means the reminder parts. It will be related to the improvement of the performance that orbits contributing the particle transport to the LID head vary according to the collisionality.

3.3 Anomalous effect on strike point patterns

When we consider the anomalous diffusion described in subsection 2.1.3, the radial diffusion of the particles becomes strong. The anomalous diffusion affects the strike point pattern to become uniform, however, the pattern is not symmetrically distributed, see Fig. 3.13. The distribution of $v_{\parallel}/v$ is also asymmetric as shown in Fig. 3.14 and Table 3.1. These results specify the difference between the neoclassical effect and the anomalous one. According to the ratio of the mean free path to the connection length $\lambda_{\mathrm{mfp}}/L_{\mathrm{c}}$, the orbits of the particles contributing the transport vary. On the other hand, the anomalous effect is independent of the orbits and the transition between passing and trapped particle orbits. The field line tracing code coupled to a random walk process is used to exclude the neoclassical effect, and the strike point pattern is shown in Fig. 3.15. The strike point pattern is symmetry in almost complete. Thus, the numerical results given in the present paper signify the important role of the neoclassical effect in the estimation of the particle transport under HT-operation, even if the anomalous diffusion makes the strike point patterns uniform.

$R_{\rm ax}$ [m]	$\lambda_{\rm mfp}/L_{\rm c}$	D_a [m^2/s]	remarks	head (total=1.0)		head (total=1.0)	
				front	rear	$v_\parallel/v<0$	$v_\parallel/v>0$
3.60	0.03	0	$E=300$ eV see Fig. 3.5	0.6	0.4	0.6	0.4
		0	$E=300$ eV no error-field	0.7	0.3	0.6	0.4
	0.3	0	$E=300$ eV see Fig. 3.1	0.2	0.8	0.7	0.3
		0	$E=300$ eV no error-field	0.3	0.7	0.7	0.3
		0.1	$E=300$ eV see Fig. 3.11	0.3	0.7	0.6	0.4
		1.0	$E=300$ eV	0.4	0.6	0.6	0.4
	3	0	$E=300$ eV see Fig. 3.4	0.1	0.9	0.6	0.4
3.75	0.03	0	$E=300$ eV	0.4	0.6	0.7	0.3
	0.3	0	$E=300$ eV	0.1	0.9	0.7	0.3
	3	0	$E=300$ eV	0.1	0.9	0.5	0.5

Table 3.1: Ratios of the test particles striking the LID head. The term "front" means the ratio of the test particles striking the front part of the head which is shown in the front-view of the strike point pattern. The term "rear" means the ratio of the test particles striking the reminder parts. The term "$v_\parallel/v<0$" ("$v_\parallel/v>0$") means the ratio of the particles having $v_\parallel/v<0$ ($v_\parallel/v>0$), which strike the head.

$R_{\rm ax}$ [m]	$\lambda_{\rm mfp}/L_{\rm c}$	$D_{\rm a}$ [m^2/s]	remarks	front (total = 1.0)		rear (total = 1.0)	
				$v_\parallel/v < 0$	$v_\parallel/v > 0$	$v_\parallel/v < 0$	$v_\parallel/v > 0$
3.60	0.03	0	$E = 300$ eV see Fig. 3.5	0.5	0.5	0.8	0.2
		0	$E = 300$ eV no error-field	0.5	0.5	0.7	03
	0.3	0	$E = 300$ eV see Fig. 3.1	0.7	0.3	0.8	0.2
		0	$E = 300$ eV no error-field	0.6	0.4	0.8	0.2
		0.1	$E = 300$ eV see Fig. 3.11	0.6	0.4	0.7	0.3
		1.0	$E = 300$ eV	0.5	0.5	0.6	0.4
	3	0	$E = 300$ eV see Fig. 3.4	0.7	0.3	0.6	0.4
3.75	0.03	0	$E = 300$ eV	0.5	0.5	0.8	0.2
	0.3	0	$E = 300$ eV	0.7	0.3	0.7	0.3
	3	0	$E = 300$ eV	0.6	0.4	0.5	0.5

Table 3.2: Ratios of the test particles striking the front and rear parts of the LID head. The term "$v_\parallel/v < 0$" ("$v_\parallel/v > 0$") means the ratio of the particles having $v_\parallel/v < 0$ ($v_\parallel/v > 0$), which strike the front or rear part of the head.

$\lambda_{\rm mfp}/L_{\rm c}$	trapped	passing
0.03	0.3	0.7
0.3	0.2	0.8
3	0.1	0.9

Table 3.3: Ratios of trapped and passing the test particles strike the LID head.

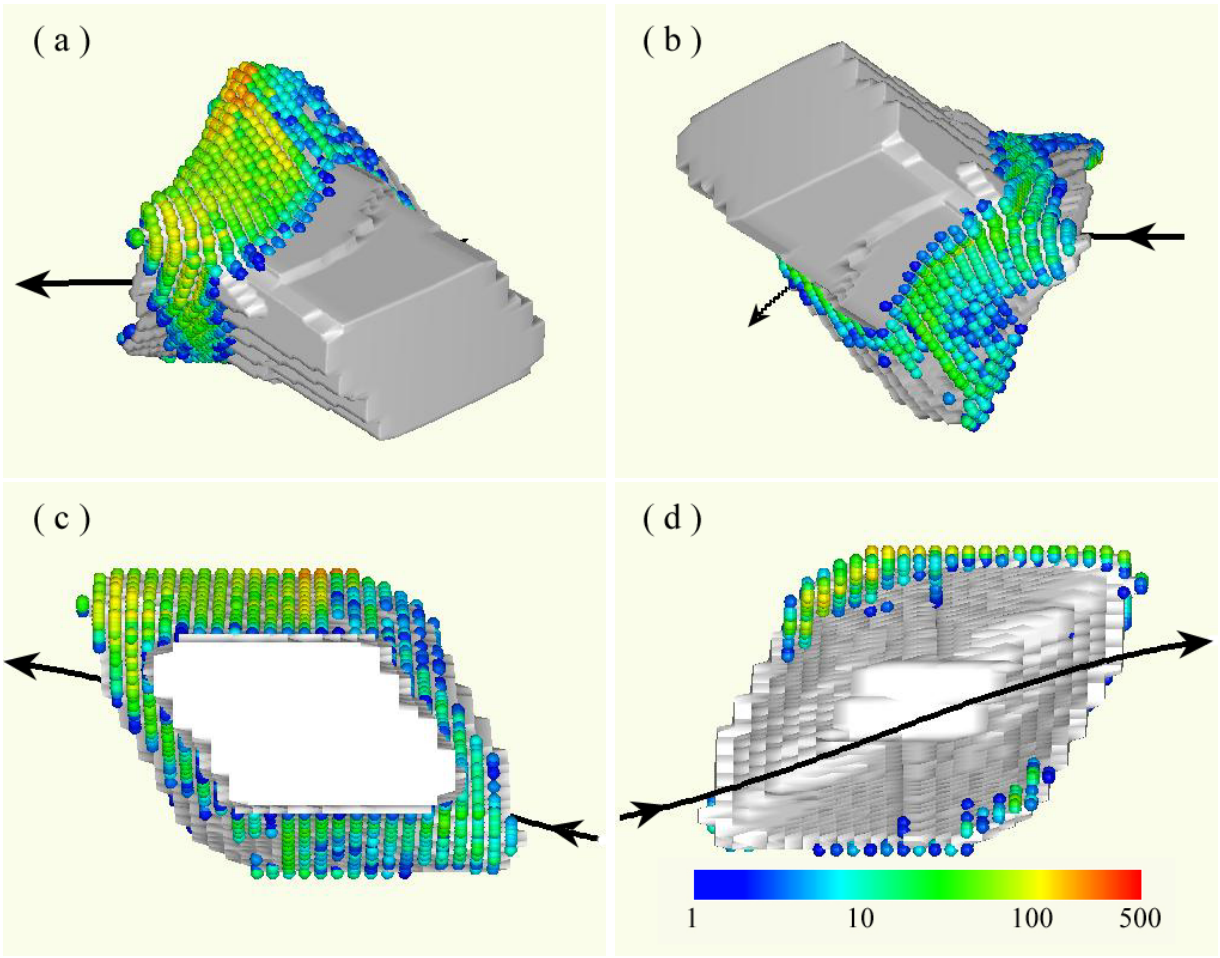

Figure 3.1: The strike point pattern on the LID head for the case of $R_{\rm ax} = 3.6$ m, $E = 300$ eV and $\lambda_{\rm mfp}/L_{\rm c} \approx 0.3$; (a) the slanting-rear-view of the pattern, (b) the opposite-side-view of the figure (a), (c) the rear-view of the pattern, (d) the front-view of the pattern. The color of the pattern indicates strength (A.U.) of the number of test particles striking the head. The colored pattern is plotted every 0.5 degrees for the toroidal direction. A black line indicates the orbit of the O-point of the $m/n = 1/1$ island.

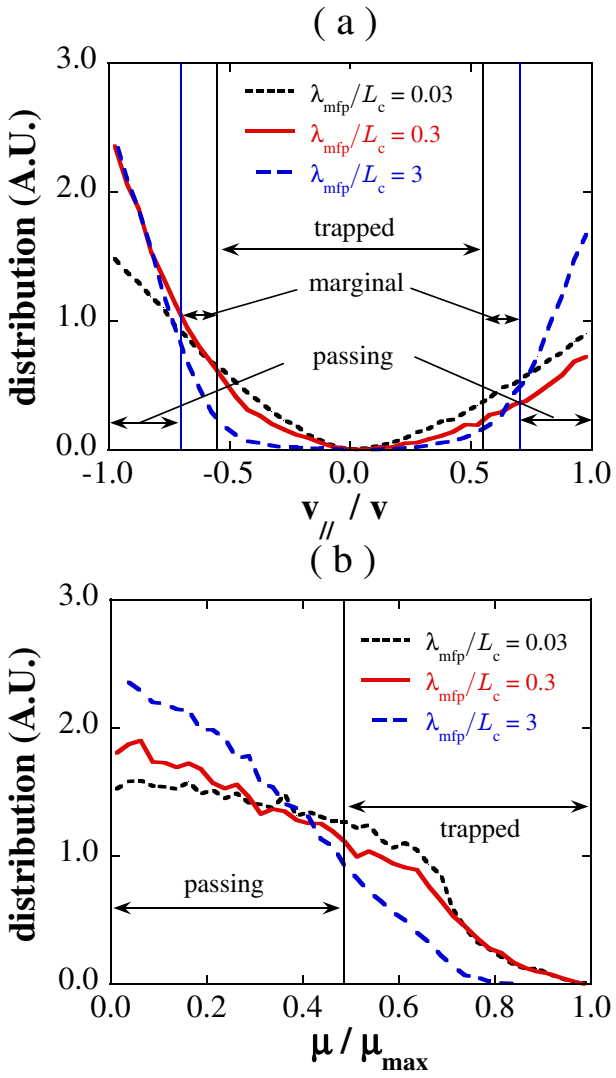

Figure 3.2: (a) The distributions of the cosine of pitch angles $v_{\parallel}/v$ of the test particles striking the head and (b) the distributions of the normalized magnetic moment of the test particles striking the head; 1) dotted black line for $\lambda_{\rm mfp}/L_{\rm c} \approx 0.03$, 2) solid red line for $\lambda_{\rm mfp}/L_{\rm c} \approx 0.3$, and 3) dashed blue line for $\lambda_{\rm mfp}/L_{\rm c} \approx 3$.
where $R_{\rm ax} = 3.6$ m and $E = 300$ eV.

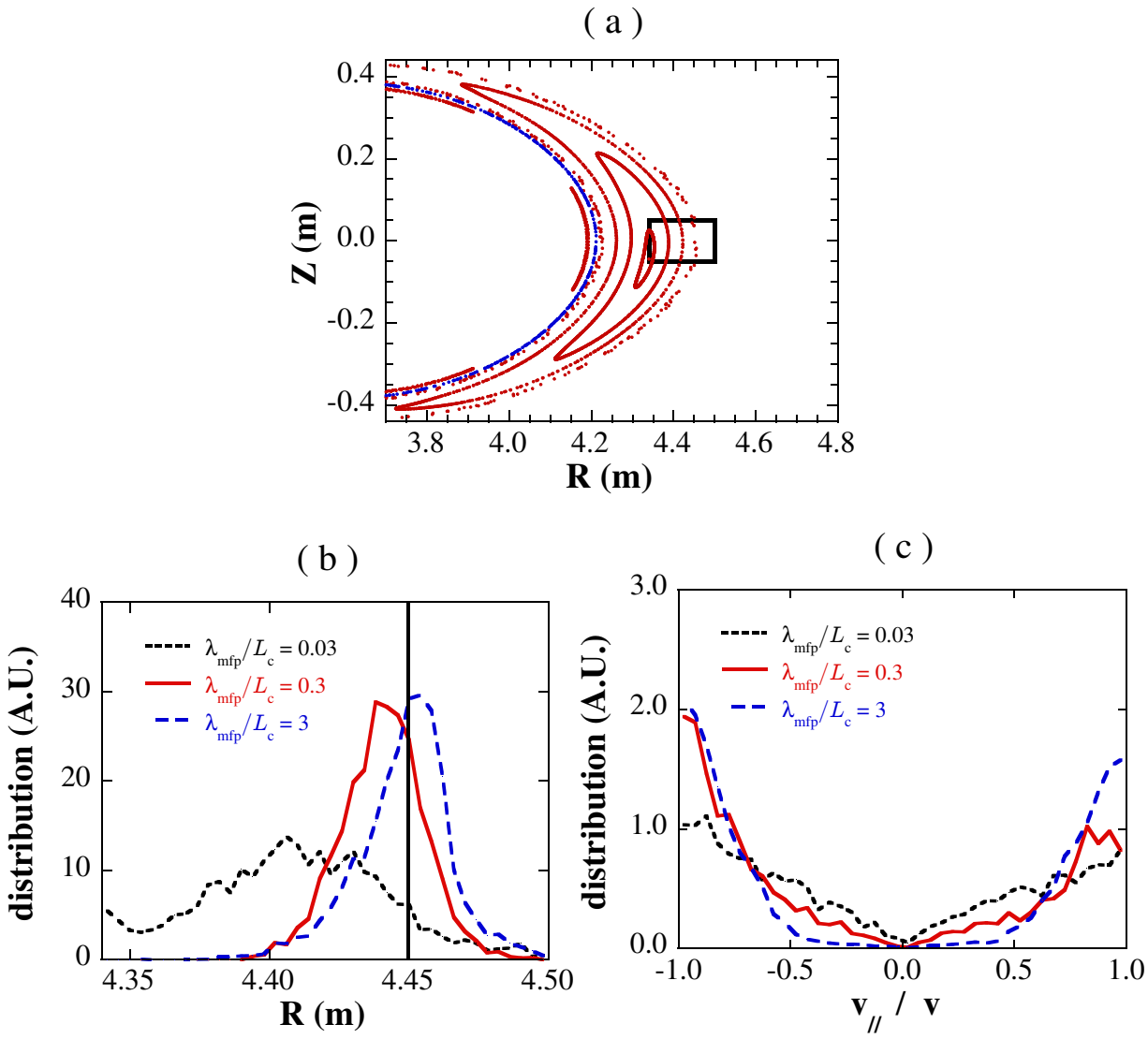

Figure 3.3: (a) The cross section is sketched by a black rectangle, on which the distributions in the figures (b) and (c) are observed. The Poincaré plots of the field lines and the magnetic flux surface where the test particles originate are shown by red and blue dots, respectively. (b) The distribution of test particles in configuration space and (c) the distribution of the cosine of pitch angles $v_{\parallel}/v$ are obtained just after the test particles starting from their initial positions go across the island separatrix; 1) dotted black line for $\lambda_{\rm mfp}/L_{\rm c} \approx 0.03$, 2) solid red line for $\lambda_{\rm mfp}/L_{\rm c} \approx 0.3$, and 3) dashed blue line for $\lambda_{\rm mfp}/L_{\rm c} \approx 3$, where $R_{\rm ax} = 3.6$ m and $E = 300$ eV. Here, a solid black line in the figure (b) indicates the averaged positions of the island separatrix on the cross section. The ergodic region is located outside the solid black line in the figure (b).

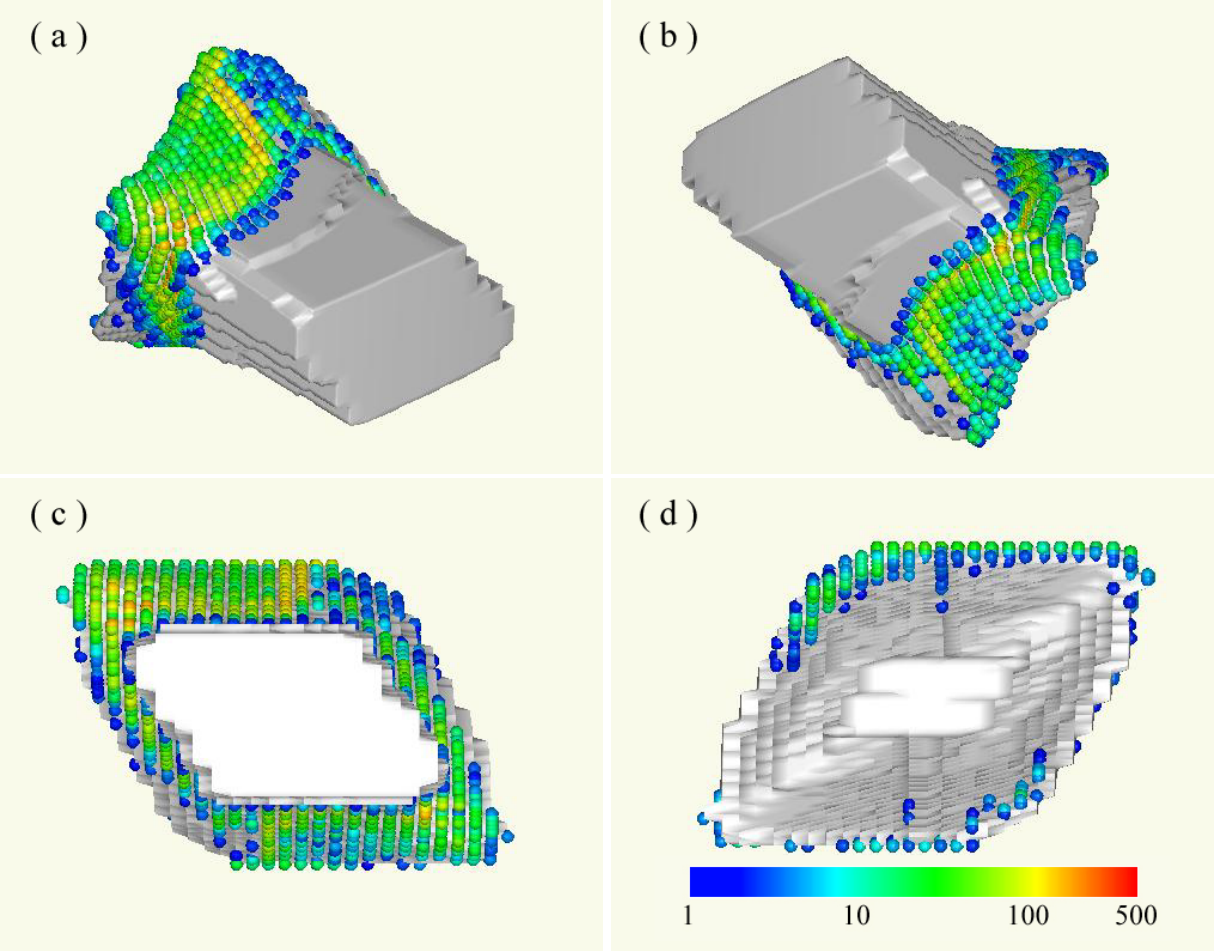

Figure 3.4: The strike point pattern for the case of $R_{\mathrm{ax}} = 3.6$ m, $E = 300$ eV and $\lambda_{\mathrm{mfp}}/L_{\mathrm{c}} \approx 3$.

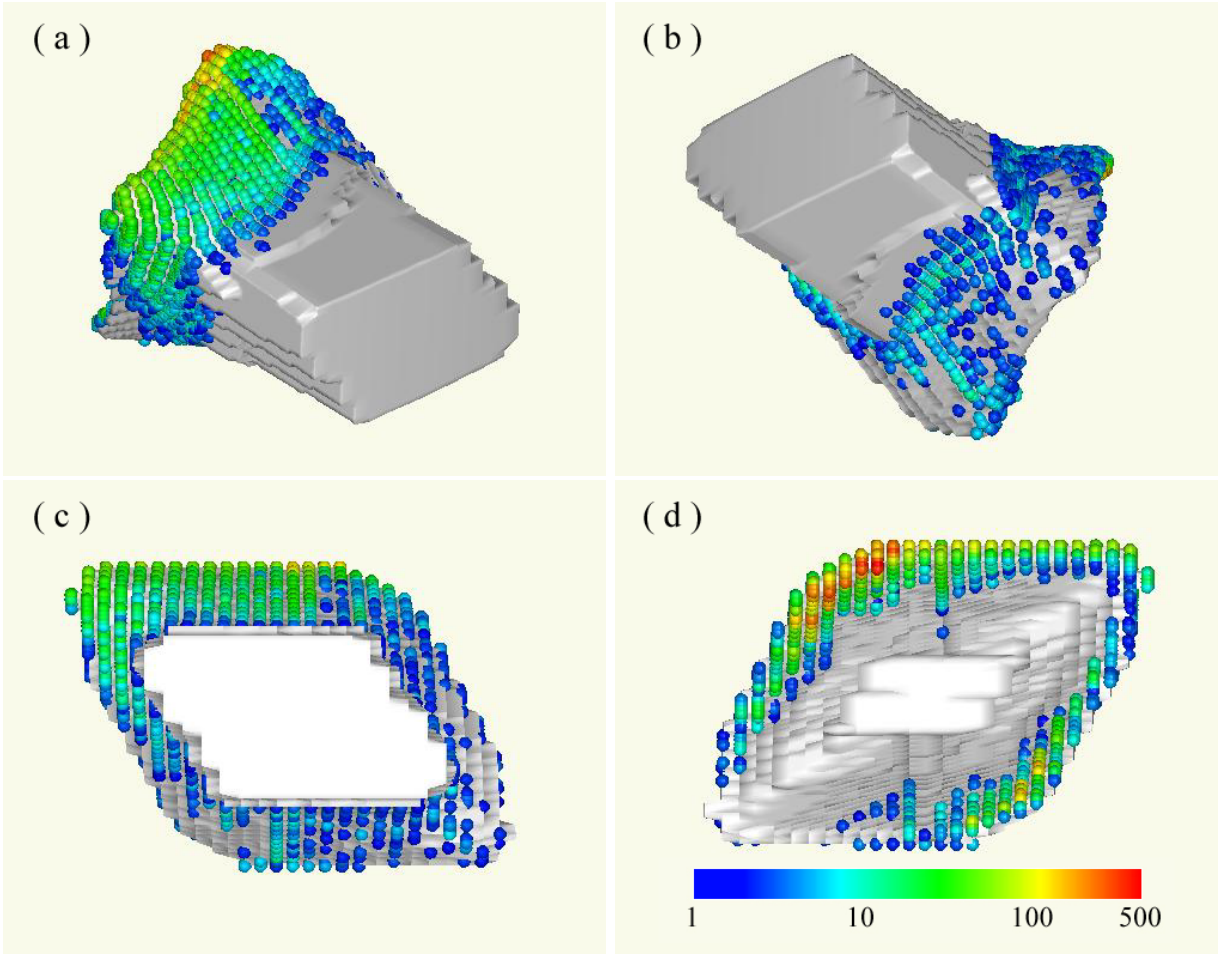

Figure 3.5: The strike point pattern for the case of $R_{\mathrm{ax}} = 3.6$ m, $E = 300$ eV and $\lambda_{\mathrm{mfp}}/L_{\mathrm{c}} \approx 0.03$.

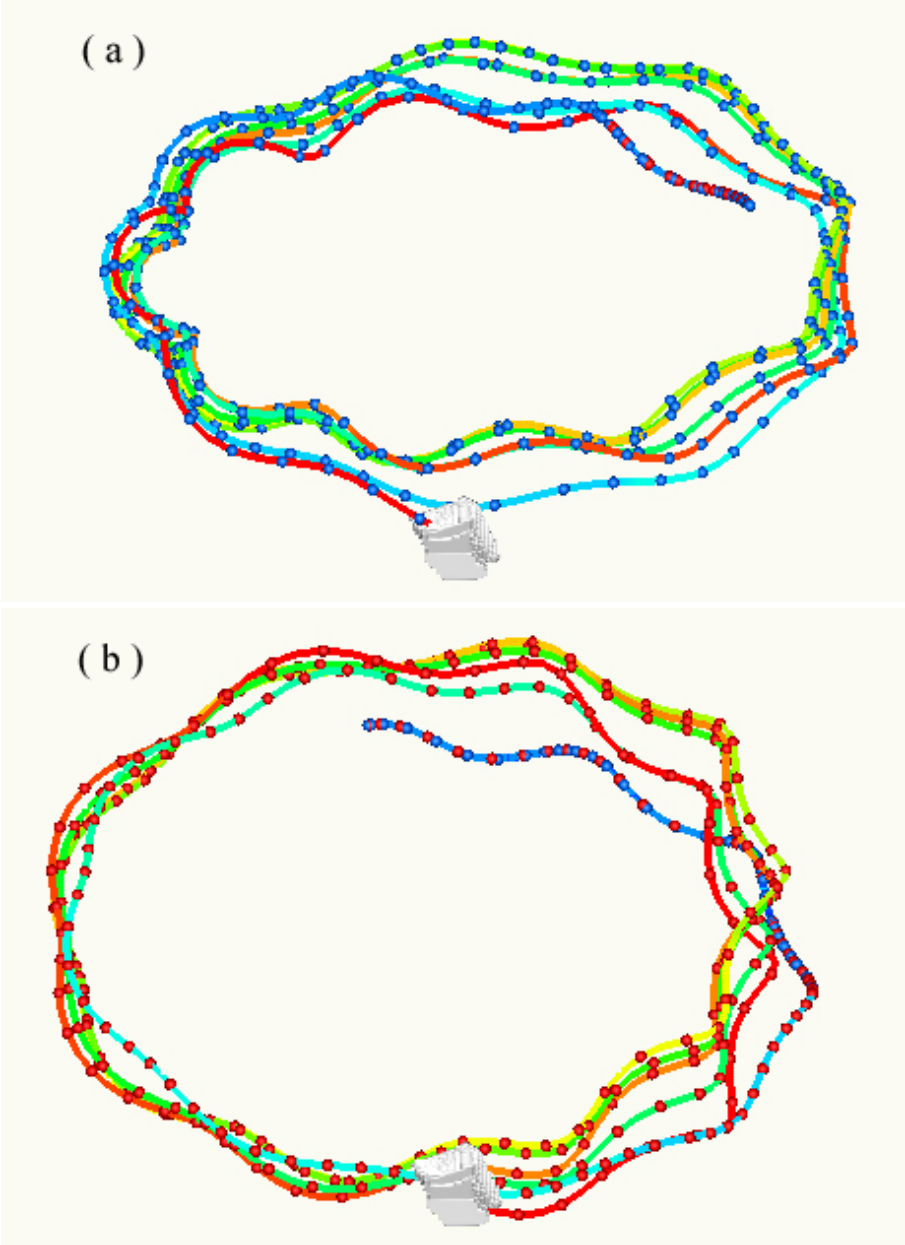

Figure 3.6: Example of orbit for $\lambda_{\rm mfp}/L_{\rm c} \approx 3$; (a) the orbit that strikes the head with negative pitch angle, (b) the orbit that strikes the head with positive pitch angle. The spheres are the particle positions of each step, and the color means the direction to the field lines in the pitch angle, red is the positive direction, blue is the negative direction. The line means the orbit, and the color corresponds to time. It starts from blue, and ends in red.

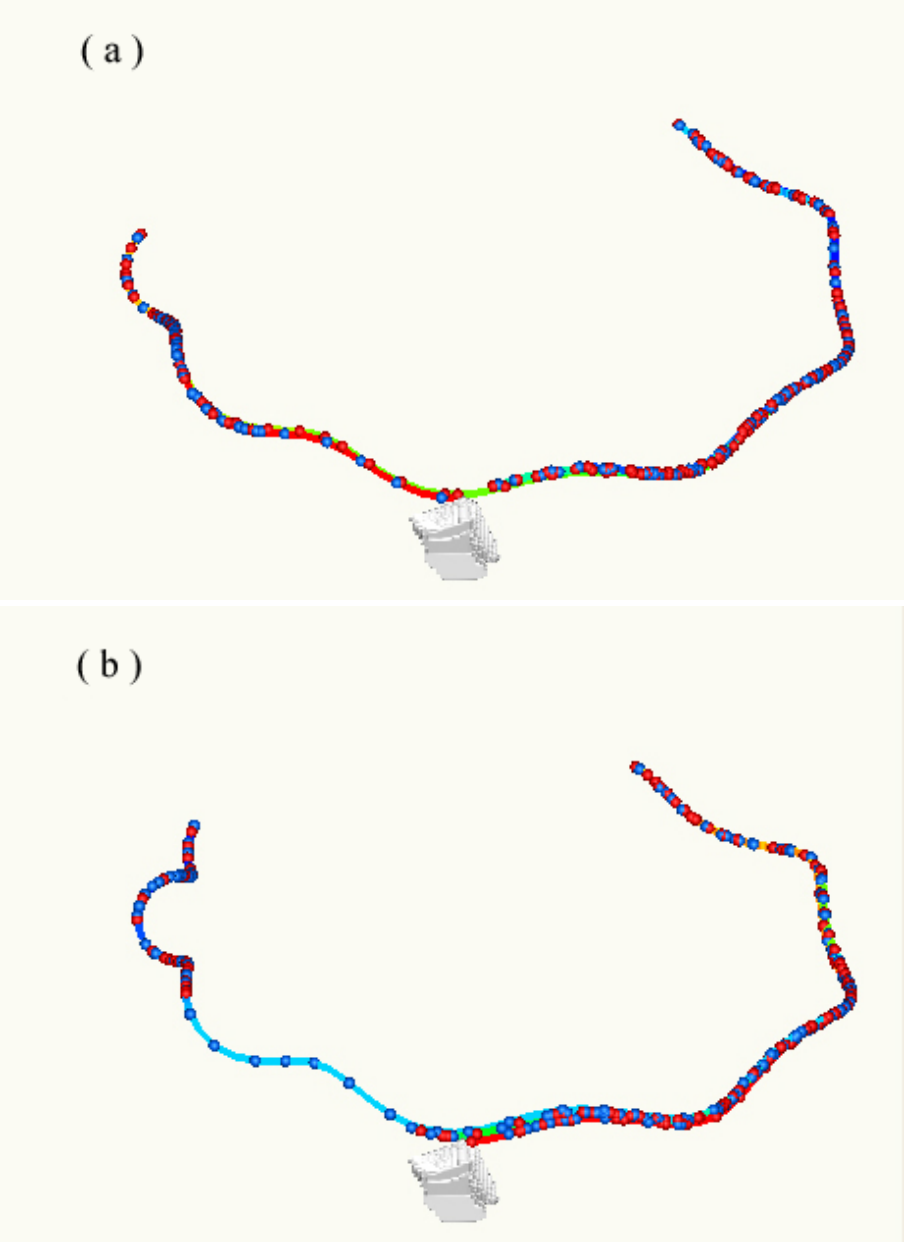

Figure 3.7: Example of orbit for $\lambda_{\mathrm{mfp}}/L_{\mathrm{c}} \approx 0.03$; (a) the orbit that strikes the head with negative pitch angle, (b) the orbit that strikes the head with positive pitch angle.

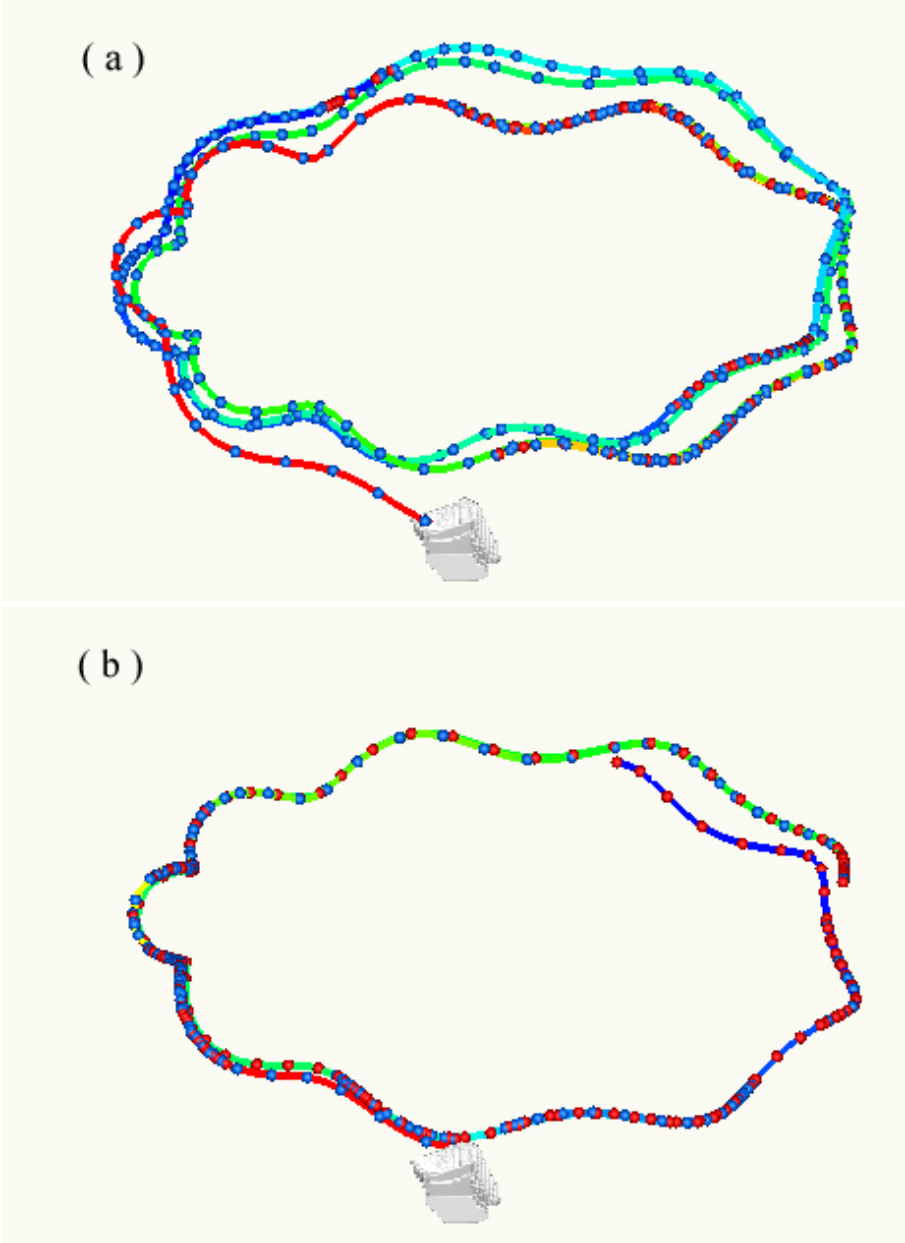

Figure 3.8: Example of orbit for $\lambda_{\mathrm{mfp}}/L_{\mathrm{c}} \approx 0.3$; (a) the orbit that turns toroidal, (b) the orbit that deeply trapped.

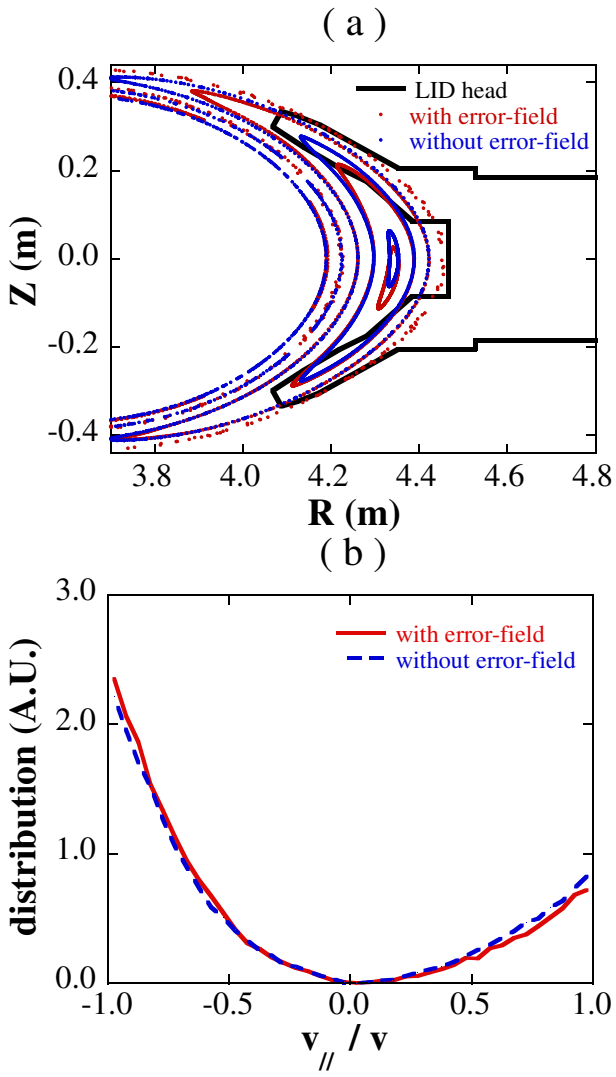

Figure 3.9: (a) Poincaré plots of field lines of the vacuum magnetic field with and without error magnetic fields for the case of $R_{\rm ax} = 3.6$ m. (b) Distributions of the cosine of pitch angles $v_{\|}/v$ of the test particles striking the head with and without error magnetic fields for the case of $R_{\rm ax} = 3.6$ m and $E = 300$ eV.

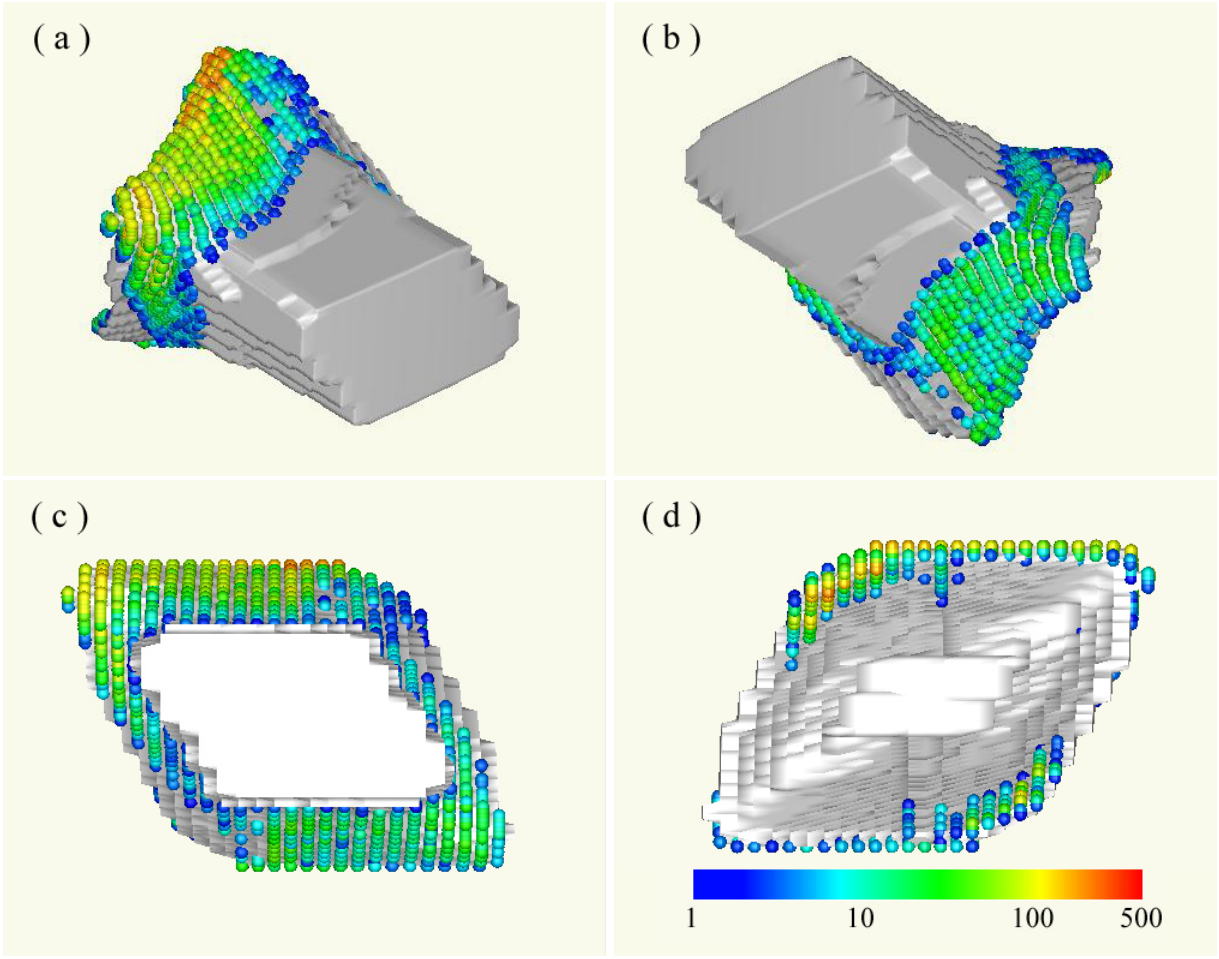

Figure 3.10: The strike point pattern for the case of $R_{\mathrm{ax}} = 3.6$ m, $E = 300$ eV $\lambda_{\mathrm{mfp}}/L_{\mathrm{c}} \approx 0.3$, and no-error field.

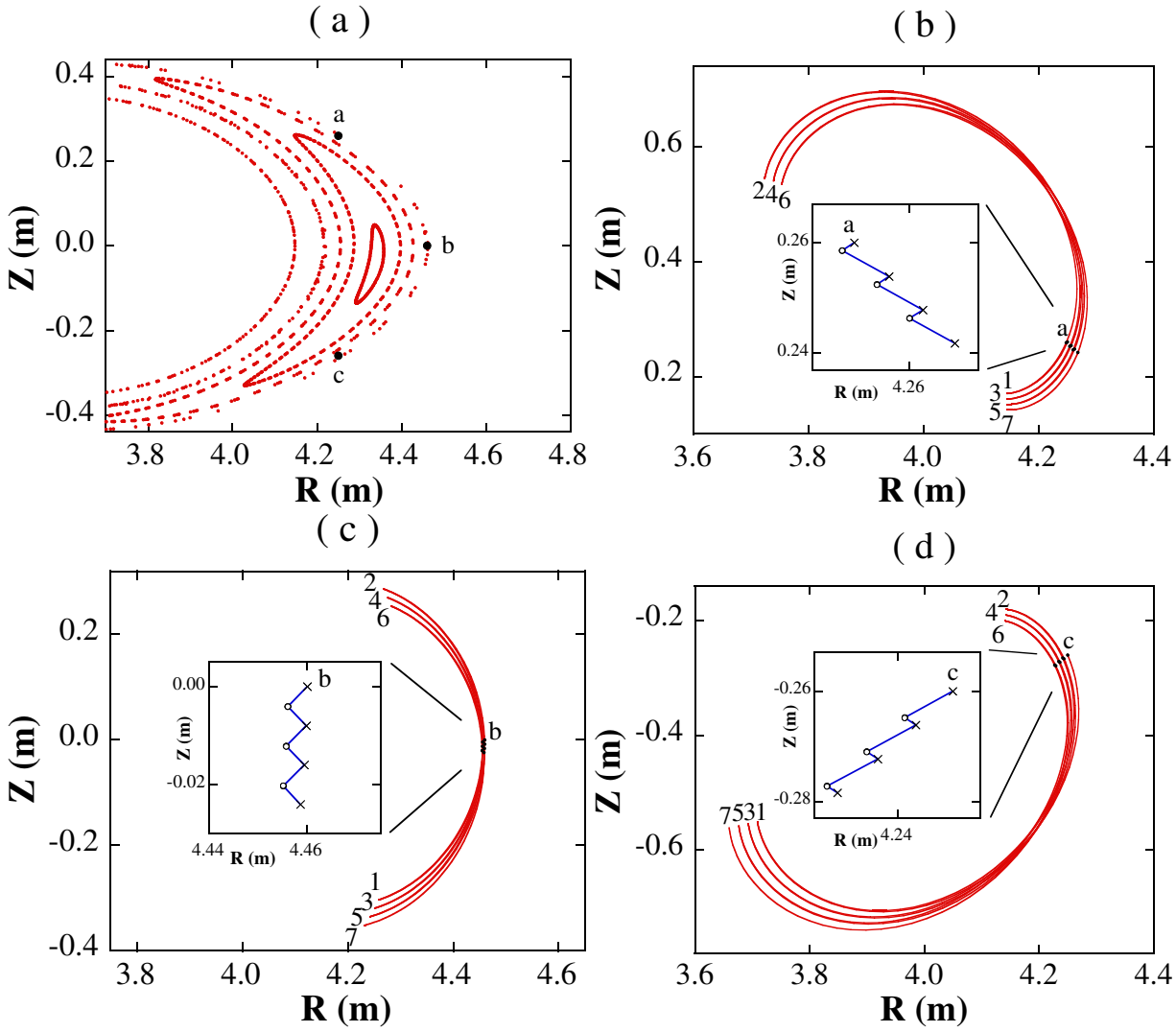

Figure 3.11: Projection of guiding center orbits onto the R-Z plane, where $R_{\rm ax} = 3.6$ m, $E = 300$ eV, and $v_\parallel/v = -0.25$ at the start points of the orbits. (a) Illustration of the Poincaré plots of the field lines (red dots) and the start points of the orbits (black dots) indicated by alphabets a-c. (b)-(d) Illustration of guiding center orbits (solid red lines) projected onto the R-Z plane. The bounce points of each orbit are given numbers in sequence. The Poincaré plots of each orbit onto the cross section given in the figure (a) are shown by black dots. The expanded illustration of the Poincaré plots of each orbit is shown in each sub-figure, where $\times$ indicates the plot having the direction of the orbit from the face to the back of this paper printed these figures and $\circ$ indicates the plot having the opposite direction to the former. Here, the plots are connected by blue lines in sequence.

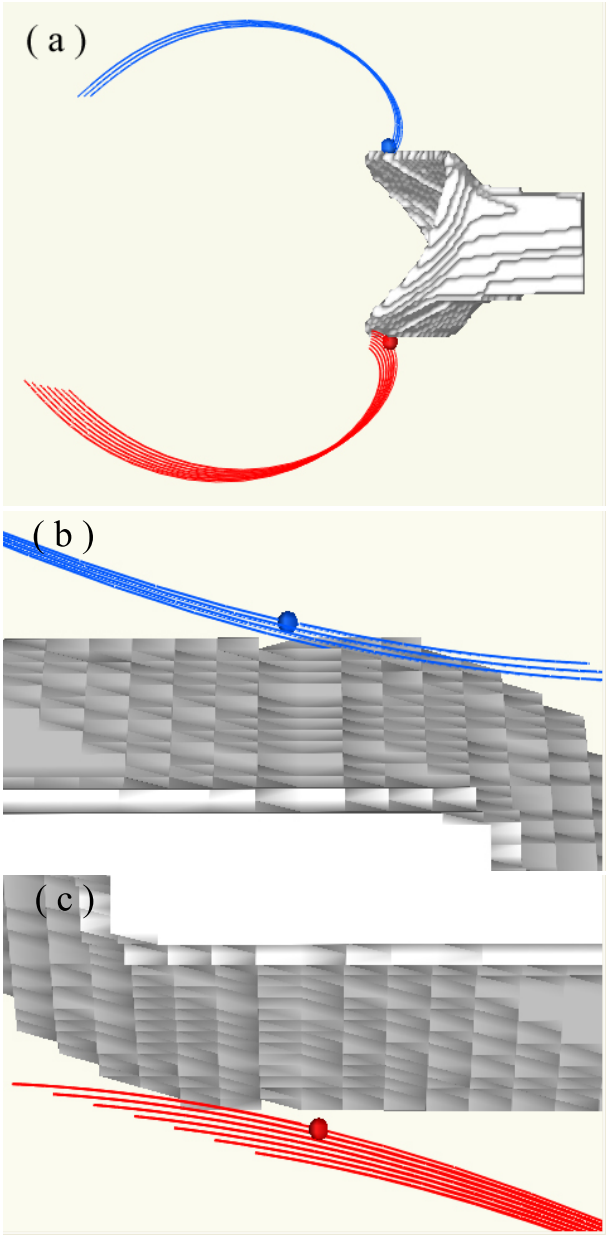

Figure 3.12: Illustration of guiding center orbits; (a) side view, (b) closeup of back view (upper), (c) closeup of back view (lower), the spheres are the initial particle positions.

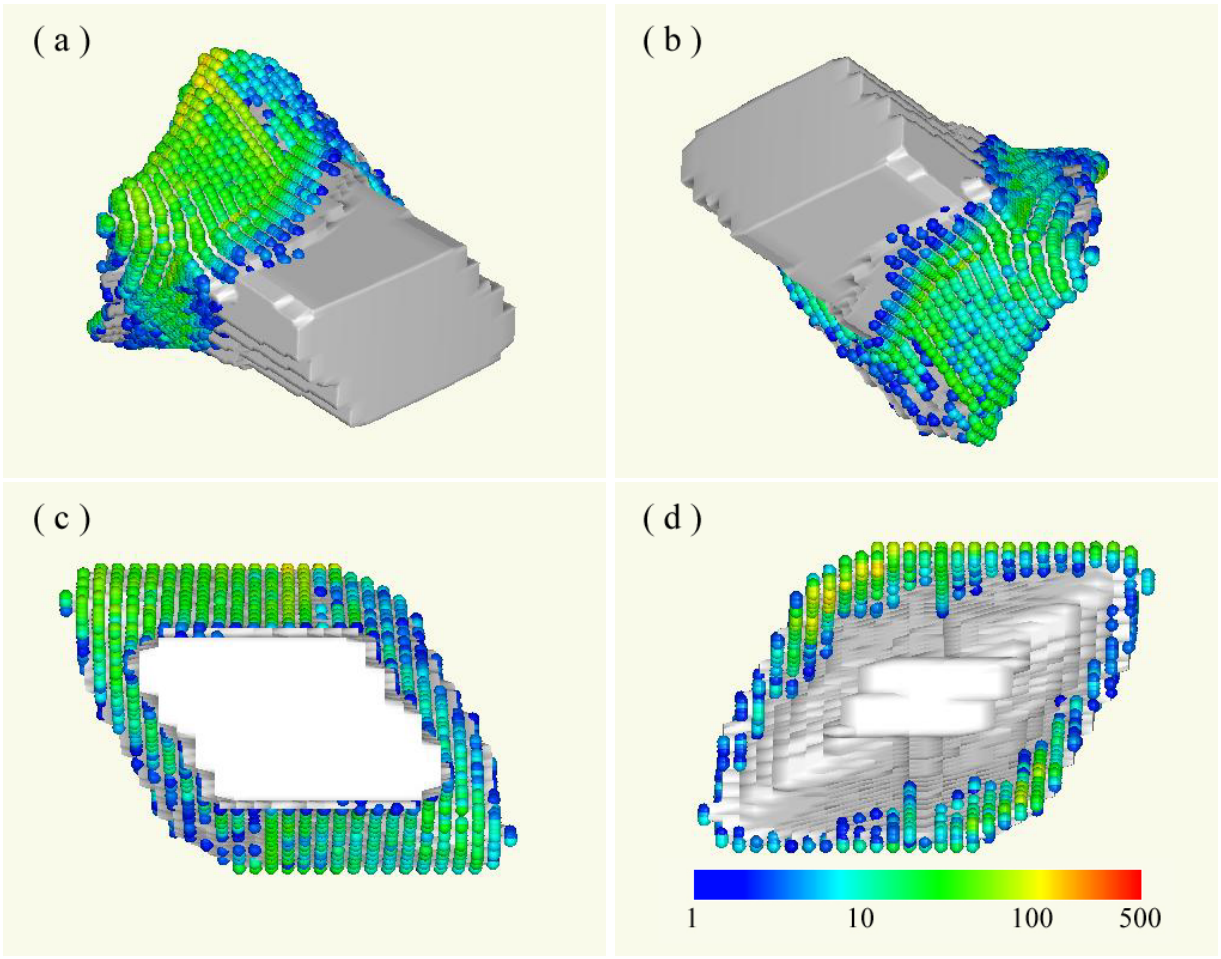

Figure 3.13: The strike point pattern for the case of $R_{\rm ax} = 3.6$ m, $E = 300$ eV and $\lambda_{\rm mfp}/L_{\rm c} \approx 0.3$. The orbits of the test particles are affected by the anomalous diffusion of $D_{\rm a} = 0.1$ m^2/s.

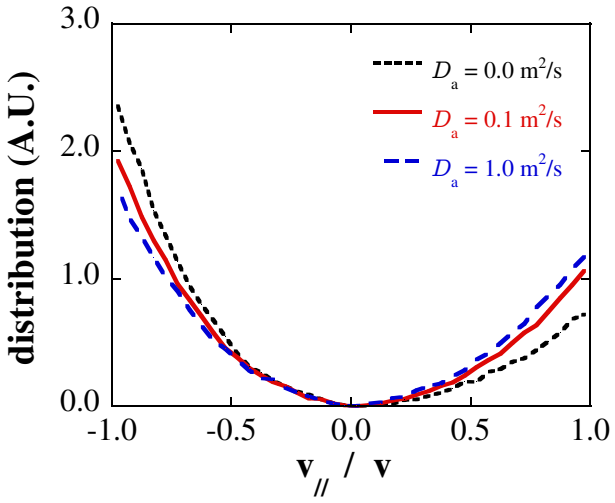

Figure 3.14: Distributions of the cosine of pitch angles $v_{\parallel}/v$ under the anomalous diffusion for the case of $R_{\rm ax} = 3.6$ m, $E = 300$ eV and $\lambda_{\rm mfp}/L_{\rm c} \approx 0.3$; (a) dotted black line for $D_{\rm a} = 0$ m^2/s, (b) solid red line for $D_{\rm a} = 0.1$ m^2/s, and (c) dashed blue line for $D_{\rm a} = 1$ m^2/s.

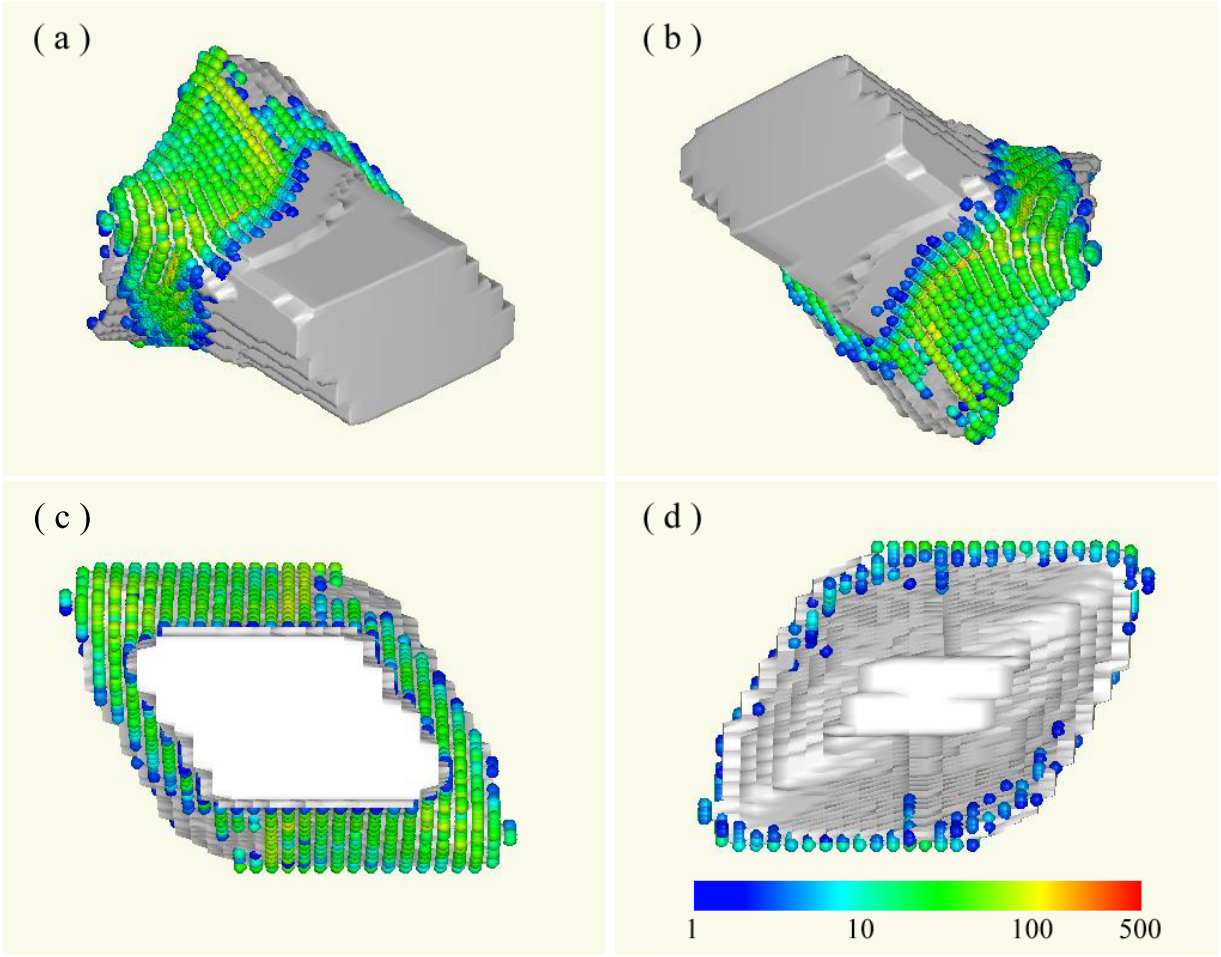

Figure 3.15: The strike point pattern for the case of the field line tracing. The orbits of the test particles are affected by the anomalous diffusion of $D_{\mathrm{a}} = 0.1$ m^2/s.

Chapter 4

Conclusion

In this thesis, we have studied the neoclassical effect on a strike point pattern in LID configuration of LHD, and have developed a Monte Carlo simulation code, MPPP(Monte carlo simulation for Particle-tracing in Peripheral Plasma), which is based on test particle representation. The pattern on the LID head is numerically observed by tracing the guiding center orbits of the test particles in the fixed magnetic field under effects of the Coulomb collision and anomalous diffusion.

First, to investigate strike point pattern of ions on the LID head we have developed Monte Carlo code solving guiding center motion in magnetic field similar to real one, and we have used the divertor head expressed by the block of computational grid similar to real one in this code. This code has been successfully benchmarked in tokamak magnetic field as shown in section 2.3. We find that the strike point patterns on the LID head are varied according to collisionality. We obtained results as follows.

We have investigated how the orbits contributing the particle transport to the LID head vary according to the collisionality. The feature of the pattern by changing $\lambda_{\rm mfp}/L_{\rm c}$ is as follows. When the mean free path $\lambda_{\rm mfp}$ is estimated as $\lambda_{\rm mfp}/L_{\rm c} \approx 0.3$, we have found that the peak of the strike point pattern is located at the edge of the head, the strike point pattern is not symmetric. For this case, the distribution of $v_{\parallel}/v$ is not symmetric either. We have found that the particle distribution in the rear side of the island has the peak inside the island separatrix, and that the test particles to the rear side of the island separatrix carry a negative momentum. On the other hand, when the mean free path

becomes larger, i.e. $\lambda_{\rm mfp}/L_{\rm c} \approx 3$ ($\nu = 9.0 \times 10^2$ s^{-1}), the strike point pattern is drastically changed, and the pattern becomes almost symmetric, and the region that the particles concentrated corresponds to the intersection of the island separatrix on the LID head. When the mean free path becomes very small, i.e. $\lambda_{\rm mfp}/L_{\rm c} \approx 0.03$ ($\nu = 7.8 \times 10^4$ s^{-1}), the test particles suffer the pitch angle scattering sufficiently and lose their initial memories when the particles go across the front side of the island separatrix, thus, the distribution of $v_{\parallel}/v$ becomes almost symmetric and has gentle slopes. The test particles intensively strike the edge of the LID head.

The classification of the particle orbit that struck on the LID head shows that the passing particle is dominant. This is because the LID head was roughly located in a magnetic well.

The example of the particle orbit shows the followings. 1) The passing particles flow along the periphery of the island. And after several toroidal turns, they reach the rear side of the island where the divertor head is placed and strike its backside. 2) The trapped particles repeat bounce motion, and they go into inside of island separatrix. They don't reach the rear side of the island, because they don't turn taurus.

When the mean free path becomes larger, i.e. $\lambda_{\rm mfp}/L_{\rm c} \approx 3$ ($\nu = 9.0 \times 10^2$ s^{-1}), the particles maintains the pitch angle for a long time for the low collision frequency, and turn toroidal many times and have not suffered trap. The passing particles flow along the periphery of the island and they reach the rear side of the island where the divertor head is placed and strike its backside. The trapped particles keep trapped and don't reach the head. In this case peak of strike point pattern corresponds to the intersection of the island separatrix on the LID head. On the other hand, when the mean free path becomes small, i.e. $\lambda_{\rm mfp}/L_{\rm c} \approx 0.03$ ($\nu = 7.8 \times 10^4$ s^{-1}), the particles frequently changes the pitch angle for high collision frequency, and trapped don't turn toroidal. Therefore, the particles escaping into the island region repeat bounce motion sufficiently and are carried to a far region from the island separatrix. In this case the particles strike mainly the inside in front of the LID head and decrease the number of particles that reach rear side separatrix, and a peak of the strike point pattern is located at the edge of the head.

And, when the mean free path is estimated as $\lambda_{\rm mfp}/L_{\rm c} \approx 0.3$ ($\nu = 8.4 \times 10^3$ s^{-1}),

the passing particles and the trapped particles exist together changing between the two. Therefore, trapped particles escape into the island region and suffer the pitch angle scattering and are carried to the inside of region from the island separatrix, moreover reaches the rear side of separatrix, and the peak of the strike point pattern is located at the edge of the head. Therefore, the strike point patterns on the LID head are varied according to collisionality.

One may suspect that the broken symmetry is caused by error magnetic fields, because the structure of the $m/n = 1/1$ magnetic island is perturbed by the error fields. As far as we have examined, however, there is no significant difference in the results even if the error fields are canceled out,

In general, trapped particle orbits located at the upper side of the island drift into the head. On the other hand, trapped particle orbits located at the lower side of the island go away from the head. Thus, the asymmetrical pattern is expected.

From the ratios of the test particles striking the front and rear parts of the LID head we have estimated the performance of the LID system. The performance is expected to be improved with increasing $\lambda_{\rm mfp}/L_{\rm c}$; i.e. the ion flux is guided mainly to the rear part of the head.

When we consider the anomalous diffusion, the radial diffusion of the particles becomes strong. The anomalous diffusion affects the strike point pattern to become uniform, although, the pattern is not symmetrically distributed. The distribution of $v_{\parallel}/v$ is also asymmetric. These results specify the difference between the neoclassical effect and the anomalous one. According to the ratio of the mean free path to the connection length $\lambda_{\rm mfp}/L_{\rm c}$, the orbits of the particles contributing the transport vary. On the other hand, the anomalous effect is independent of the orbits and the transition between passing and trapped particle orbits. Thus, the numerical results given in this study signify the important role of the neoclassical effect in the estimation of the particle transport under HT-operation, even if the anomalous diffusion makes the strike point patterns uniform.

Bibliography

[1] H. Maeda, S. Sengoku, H. Kimura, H. Ohtsuka, K. Ohasa, M. Nagami, K. Odajima, S. Yamamoto, M. Azumi, S. Kasai, T. Sugie, K. Takahashi, K. Kumagai, T. Shiji, T. Yamauchi, H. Takeuchi, T. Kawakami, A. Nagashima, A. Funahashi, K. Anno, T. Shibata, T. Arai, H. Hiratsuka, H. Sunaoshi, K. Yokoyama, Y. Shimomura in Plasma Physics and Controlled Nuclear Fusion Research (*Proc. 7th Int. Conf.,Innsbruck,*1978) Vol.1 IAEA, Vienna 377 (1979).

[2] ITER Physics Expert Group on Divertor, ITER Physics Expert Group on Divertor Modelling and Database, ITER Physics Basis, ITER EDA, Chapter.4: Power and particle control, Nuclear Fusion **39**, 2391 (1999).

[3] A. Loarte, Plasma Phys. Control. Fusion **43**, R183 (2001).

[4] F. Wagner, G. Becker, K. Behringer, D. Campbell, A. Eberhagen, W. Engelhardt, G. Fussmann, O. Gehre, J. Gernhardt, G. v. Gierke, G. Haas, M. Huang, F. Karger, M. Keilhacker, O. Klüber, M. Kornherr, K. Lackner, G. Lisitano, G. G. Lister, H. M. Mayer, D. Meisel, E. R. Müller, H. Murmann, H. Niedermeyer, W. Poschenrieder, H. Rapp, H. Röhr, F. Schneider, G. Siller, E. Speth, A. Stäbler, K. H. Steuer, G. Venus, O. Vollmer, and Z. Yü, Phys. Rev. Lett. **49**, 1408 (1982).

[5] F. Wagner, M. Keilhacker and the ASDEX and NI Team, J. Nucl. Mater. **121** 103 (1984).

[6] J. Luxson, P. Anderson, F. Batty, C. Baxi, G. Bramson, N. Brooks, B. Buuley, K.H. Burrel, R. Callis, G. Campbell, T. Calstrom, A. Colleraine, J. Cummings, L. Davis, J. DeBoo, S. Ejima, R. Evanko, H, Fukumoto, R. Gallix, J. Gilleland, T. Glad P. Gohil,

A. Gootgeld, R. J. Groebner, S. Hanei, J. Haskovec, E. Heckman, M. Heiberger, F.J. Helton, P. Henline, D. Hill, D. Hoffman, E. Hoffmann, R. Hong, N. Hosogane, C. Hsieh, G.L. Jackson, G.Jahns, G. Janeschitz, E. Johnson, A. Kellman, J.S. Kim, J. Kohli, A. Langhorn, L. Lao, P. Lee, S. Lightner, J. Lohr, M. Mahdavi, M. Mayberry, B, McHarg, T. McKelvey, R. Milley, C.P. Moeller, D. Moore, A. Nerem, P. Noil, T. Okawa, N. Ohyabu, T. Osbone, D. Overski, P. Peterson, T. Petrie, J. Phillps, R. Prater, J. Rawls, E. Reis, D. Remsen, T. Riedy, P. Rock, K. Schaubel, D. Schissel, J. Scoville, R. Seraydarin, M. Shimada, T. Shoji, B. Sleaford, J. Smith Jr.,P Smith, P.T. Shider, R.D. Stambaugh, R. Stav, H.St. John, R. Stockdale, E.J. Strait, R, Street, T.S. Taylor, J. Tooker, M. Tupper, S.K. Wong, S. Yamaguchi, in Plasma Physics and Controlled Nuclear Fusion Research (*Proc. 11th Int. Conf.,Kyoto,*1986) Vol.1 IAEA, Vienna 159 (1987).

[7] M.R. Wade, W.P. West, R.D. Wood, S.L. Allen, J.A. Boedo, N.H. Brooks, M.E. Fenstermacher, D.N. Hill, J.T. Hogan, R.C. Isler, G.L. Jackson, C.J. Lasnier, R. Lehmer, A.W. Leonard, M.A. Mahdavi, R. Maingi, R.A. Moyer, T.H. Osborne, T.W. Petrie, M.J. Schaffer, R.D. Stambaugh, J.G. Watkins and D.G. Whyte, J. Nucl. Mater. **266-269** 44 (1999).

[8] O. Gruber, A. Kallenbach, M. Kaufmann, K. Lackner, V. Mertens, J. Neuhauser, F. Ryter, H. Zohm, M. Bessentrodt-Weberpals, K. Büchl, S. Fiedler, A. Field, Ch. Fuchs, C. Garcia-Rosales, G. Haas, A. Herrmann, W. Herrmann, S. Hirsch, W. Köppendörfer, P. Lang, G. Lieder, K.-F. Mast, C.S. Pitcher, M. Schittenhelm, J. Stober, W. Suttrop, M. Troppmann, M. Weinlich, M. Albrecht, M. Alexander, K. Asmussen, M. Ballico, K. Behler, K. Behringer, H.S. Bosch, M. Brambilla, A. Carlson, D. Coster, L. Cupido, H.J. DeBlank, S.De Pena Hempel, S. Deschka, C. Dorn, R. Drube, R. Dux, A. Eberhagen, W. Engelhardt, H.-U. Fahrbach, H.-U. Feist, D. Fieg, G. Fußmann,O. Gehre, J. Gernhardt, P.Ignacz, B. Jüttner, W. Junker, T. Kass, K. Kiemer, H.Kollotzek, M. Kornherr, K. Krieger, B. Kurzan, R. Lang, M. Laux, M. E. Manso, M. Maraschek, H.-M.Mayer, P. McCarthy, D. Meisel, R.Merkel, H. Murmann, B. Napiontek, D.Naujoks, G. Neu, R. Neu, J.-M. Noterdaeme, G. Pautasso, W. Poschenrider, G. Raupp, H.

Richter, T. Richter, H. Röhr, J. Roth, N. Salmon, H. Salzmann, W. Sandmann, H.-B. Schilling, H. Schneider, R. Schneider, W. Scheider, K. Schönmann, G. Schramm, U. Schumacher, J. Schweinzer, U. Seidel, F. Serra, A. Silva, M. Sokoll, E. Speth, A. Stäbler, K.-H. Steuer, B. Streibl, W. Treutterer, M. Ulrich, P. Varela, H. Vernickel, O. Vollmer, H. Wedler, U. Wenzel, F. Wesner, R. Wunderlich, D. Zasche and H.P Zehrfeld, Phys. Rev. Lett. **74**, 4217 (1995).

[9] Ohyabu N, Kakuyugo-Kenkyu **66** 525. (1991).

[10] N. Ohyabu, K. Yamazaki, I. Katanuma, Hantao JI, T. Watanabe, K. Watanabe, H. Kano, K. Akaishi, T. Ono, H. Kaneko, T. Kawamura, Y. Kubota, N. Noda, A. Sagara, O. Motojima, M. Fujiwara and A. Iiyoshi, in Plasma Physics and Controlled Nuclear Fusion Research IAEA, Vienna 605 (1992)

[11] H. Takase, and N. Ohyabu, Nuclear Fusion **35**, 123 (1995).

[12] A. Iiyoshi, M. Fujiwara, O. Motojima, N. Ohyabu, and K. Yamazaki, Fusion Tecnol. **17**, 169 (1990).

[13] O. Motojima, H. Yamada, A. Komori, N. Ohyabu, K. Kawahata, O. Kaneko, S. Masuzaki, A. Ejiri, M. Emoto, H. Funaba, M. Goto, K. Ida, H. Idei, S. Inagaki, N. Inoue, S. Kado, S. Kubo, R. Kumazawa, T. Minami. J. Miyazawa, T. Morisaki, S. Morita, S. Murakami, S. Muto, T. Mutho, Y. Nagayama, Y. Nakamura, H. Nakanishi, K. Narihara, K. Nishimura, N. Noda, T. Kobuchi, S. Ohdachi, Y. Oka, M. Osakabe, T. Ozaki, B.J. Peterson, A. Sagara, S. Sakakibara, T. Sakamoto, H. Sasao, M. Sasao, K. Sato, M. Sato, T. Seki, T. Shimozuma, M. Shoji, H. Suzuki, Y. Takeiri, K. Tanaka, K. Toi, T. Tokuzawa, K. Tsumori, K, Tsuzuki, I. Yamada, S. Yamaguchi, M. Yokoyama, K.Y. Watanabe, T. Watari, Y. Hmada, K. Matsuoka, K. Murai, K. Ohkubo, M. Fujiwara and A. Iiyoshi, Phys. Plasmas **6**, 1843 (1999).

[14] N. Ohyabu, T. Watanabe, H. Ji, H. Akao, T. Ono, T. Kawamura, K. Yamazaki, K. Akaishi, N. Inoue, A. Komori, N. Noda, A. Sagara, H. Suzuki, O. Motojima, M. Fujiwara and A. Iiyoshi, Nucl. Fusion **34**, 387 (1994).

[15] N. Ohyabu, J. DeGRASSIE and T. EVANS , J. Nucl. Mater. **145-147** 844 (1987).

[16] A. Komori, N. Ohyabu, T.Watanabe, H. Suzuki, A. Sagara, N. Noda, K. Akaishi, N. Inoue, Y. Kubota, O. Motojima, M. Fujiwara and A. Iiyoshi, in Plasma Physics and Controlled Fusion Research, IAEA, Vienna 773 (1995).

[17] A. Komori, N. Ohyabu, A.C. England, D.E. Greenwiood, N. Inoue, C.C. Klepper, S. Kubo D.K. Lee, J.F. Lyon, S. Masuzaki, T. Minami, T. Morisaki, S. Morita, K. Nisimura, S. Ohdachi, S. Okamura, D.R. Overbey, J.A. Rome, S. Sakakibara, D.E. Schechter, H. Suzuki, C. Takahashi, K. Tanaka, K. Watanabe, T. Watanabe, C.T. Wilson, H. Yamada, A. Yonezu, K. Matsuoka, O. Motojima, M. Fujiwara and A. Iiyoshi, Fusion Eng. Des. **39-40** 241 (1998).

[18] T. Morisaki, S. Masuzaki, H. Suzuki, A. Komori, N.Ohyabu, O. Motojima, S. Okamura, K. Matsuoka, LHD Expermental Group and CHS Group, Fusion Eng. Des. **65** 475 (2003).

[19] N. Ohyabu, J. Plasma and Fusion Res. **71**, 1238 (1995).

[20] N. Ohyabu, A. Komori, K. Akaishi, N. Inoue, Y. Kubota, A. I. Livshits, N. Noda, A. Sagara, H. Suzuki, T. Watanabe, O. Motojima, M. Fujiwata and A. Iiyoshi J. Nucl. Mater. **220-222** 298 (1995).

[21] N. Ohyabu, A. Komori, H. Suzuki, T. Morisaki, S. Masuzaki, H. Funaba, N. Noda, Y. Nakamura, A. Sagara, N. Inoue, R. Sakamoto, S. Inagaki, S. Morita, Y. Takeiri, T. Watanabe, O. Motojima, M. Fujiwara and A. Iiyoshi, J. Nucl. Mater. **266-269** 302. (1999).

[22] A. Komori, N. Ohyabu, S. Masuzaki, T. Morisaki, H. Suzuki, C. Takahashi, S. Sakakibara, K. Watanabe, T. Watanabe, T. Minami, S. Morita, K. Tanaka, S. Ohdachi, S. Kubo, N. Inoue, H. Yamada, K, Nishimura, S. Okamura, K. Matsuoka, O. Moyojima, M. Fujiwara and A. Iiyoshi, in Plasma Physics and Controlled Fusion Research, IAEA, Vienna 3 (1997)

[23] A. Komori, N. Ohyabu, S. Masuzaki, T. Morisaki, H. Suzuki, C. Takahashi, S. Sakakibara, K. Watanabe, T. Watanabe, T. Minami, S. Morita, K. Tanaka, S. Ohdachi, S. Kubo, N. Inoue, H. Yamada, K. Nishimura, S. Okamura, K. Matsuoka, O. Motojima, M. Fujiwara, A. Iiyoshi, C. C. Klepper, J. F. Lyon, A. C. England, D. E. Greeneood, D. K. Lee, D. R. Overbey, J. A. Rome, D. E. Schechter, C. T. Wilson, J. Nucl. Mater. **241-243** 967 (1997).

[24] S. Masuzaki, A. Komori, T. Morisaki, N. Ohyabu, H. Suzuki, T. Minami, S. Morita, K, Tanaka, S. Ohdachi, S. Kubo, S. Okamura, K. Matsuoka, O. Motojima, C. Klepper, J. Lyon, A. England, J. Plasma Fusion Res. 1 310 (1998).

[25] T. Morisaki, S. Masuzaki, H. Suzuki, K. Nishimura, H. Hayashi, H. Yonezu, A. Komori, N. Ohyabu and O. Motojima, J. Plasma Fusion Res. 3 188 (2000).

[26] A. Komori, T. Morisaki, R. Sakamoto, N. Ohyabu, S. Morita, B. J. Perterson, S. Masuzaki, H. Suzuki, M. Shoji, Y. Nakamura, S. Sakakibara, K. Narihara, N. Noda, O. Motojima, LHD Experimental Group, J. Nucl. Mater. **313-316** 1267 (2003).

[27] K. Nishimura, K. Kawahata, K. Narihara, T. Morisaki, S. Masuzaki, S. Sakakibara, K. Tanaka, LHD Experimental Group, J. Nucl. Mater. **313-316** 952 (2003).

[28] Y. Feng, F. Sardei, J. Kisslinger and P. Grigull, J. Nucl. Mater. **241-243**, 930 (1997).

[29] D. Reiter, J. Nucl. Mater. **196-198**, 80 (1992).

[30] P. C. Stangeby 200 *The Plasma Boundary of Magnetic Fusion Devices* (Institute of Physics, Bristol).

[31] I. Karatzas and S. E. Shreve, *Brownian Motion and Stochastic Calculus* (Springer, New York) (1988).

[32] A. Runov, S. V. Kasilov, N. McTaggart, R. Schneider, Nucl. Fusion **44**, S74 (2004).

[33] R. Kanno, S. Jimbo, H. Takamaru, M. Okamoto, J. Plasma Fusion Res. 6 527 (2004).

[34] S. Jimbo, R. Kanno, H. Takamaru and M. Okamoto, J. Plasma and Fusion Res. **80**, 649 (2004).

[35] R. G. Littlejohn, J. Plasma Phys. **29** 111 (1983).

[36] R. D. Hazeltine and J. D. Meiss, *Plasma Confinement*(Addison-Wesley Publishing Co.,1992)

[37] A. H. Boozer and G. Kuo-Petravic Phys. Fluids **24** 851 (1981)

[38] P. E. Kloeden and E. Platen *Numerical Solution of Stochastic Differential Equations* (Springer, Berlin) (1999).

[39] K. Harafuji, T. Hayashi and T. Sato J. Comput. Phys. **81** 169 (1989).

[40] W. Lotz, and J. Nührenberg, J. Phys. Fluids **31** 2984 (1988).

[41] K. Ida, N. Ohyabu, T. Morisaki, Y. Nagayama, S. Inagaki, K. Itoh, Y. Liang, K. Narihara, A. Yu. Kostioukov, B. J. Peterson, K. Tanaka, T. Tokuzawa, H. Suzuki, A. Komori and LHD Experimental Group, Phys. Rev. Lett. **88** 015002 (2002).